npj | computational materials

Article

Published in partnership with the Shanghai Institute of Ceramics of the Chinese Academy of Sciences

https://doi.org/10.1038/s41524-024-01476-3

Building up accurate atomistic models of biofunctionalized magnetite nanoparticles from first-principles calculations

Paulo Siani [1,2] ✉, Enrico Bianchetti[1] & Cristiana Di Valentin[1,2] ✉

Biofunctionalized magnetite nanoparticles offer unique multifunctional capabilities that can drive nanomedical innovations. Designing synthetic bioorganic coatings and controlling their molecular behavior is crucial for achieving superior performance. However, accurately describing the interactions between bio-inorganic nanosystem components requires reliable computational tools, with empirical force fields at their core. In this work, we integrate first-principles calculations with mainstream force fields to construct and simulate atomistic models of pristine and biofunctionalized magnetite nanoparticles with quantum mechanical accuracy. The practical implications of this approach are demonstrated through a case study of PEG (polyethylene glycol)-coated magnetite nanoparticles in physiological conditions, where we investigate how polymer chain length, in both heterogeneous and homogeneous coatings, impacts key functional properties in advanced nanosystem design. Our findings reveal that coating morphology controls polymer ordering, conformation, and polymer corona hydrogen bonding, highlighting the potential of this computational toolbox to advance next-generation magnetite-based nanosystems with enhanced performance in nanomedicine.

Iron oxide nanoparticles (IONPs), among other transition metal oxides, have gained special attention in nanomedical sciences in recent years due to their unique in vitro and in vivo biomedical applications, ranging from magnetic bioseparation, biosensing, cellular labeling, contrast agent in magnetic resonance imaging, imaging-guided therapy, hyperthermia for cancer treatment, to targeted drug delivery[1–7].

Through well-established experimental routes, the synthesis of IONPs with well-defined shapes, including spherical, cubical, octahedral, and rhombic dodecahedral, with precise control over their surface chemistry and sizes, has been successfully achieved[8–13]. Among IONPs, magnetite nanoparticles enclosed by six (001) facets, one of the most stable Fe_3O_4 surface according to Wulff construction calculations[14], are of particular interest due to their specific surface reactivity towards small organic acids[15,16], and polymers[17], enhancing their mechanical properties and colloidal stability. Polyethylene glycol (PEG) with chemically reactive terminal groups (e.g. reactive amine groups) is among the most preferred polymers for coating of IONPs, broadening their applications[18–25]. This allows, for instance, control over the molecular interactions in biological environments (e.g. protein corona) and the bioconjugation with active targeting ligands for smart drug delivery[26–29].

In synergy with experiments, computational methods through quantum mechanical (QM) calculations of iron oxide bulk electronic structure, surface chemistry and catalysis[14,30–34], mixed-resolution and multi-level calculations of Fe_3O_4/water interfaces[35–37], hybrid Monte Carlo and Molecular Dynamics (MD) simulations of bulk oxidation-state dynamics[38], and MD simulations of Fe_3O_4/organic interfaces[15,39–43], have stood out as valuable tools for obtaining molecular-level insights into Fe_3O_4-based materials. However, recent computational efforts into the development, refinement and assessment of classical force fields (FFs) for modeling Fe_3O_4 nanostructures interfacing water[44,45] and biomolecules[39,44,46] are still scarce in the literature. In this direction, Konuk et al.[39] have recently made significant contributions. They proposed a combination of the modified CLAY (mCLAY) FF, which was previously calibrated for studying the atomic-level structure of hematite/water interfaces[47] and derived from the original FF

[1]Dipartimento di Scienza dei Materiali, Università di Milano-Bicocca, via R. Cozzi 55, 20125 Milano, Italy. [2]BioNanoMedicine Center NANOMIB, Università di Milano-Bicocca, Milano, Italy. ✉e-mail: paulo.siani@unimib.it; cristiana.divalentin@unimib.it

developed for a more general class of hydrated minerals including hydroxides, oxyhydroxides, and clays[48], with the biomolecular General AMBER FF (GAFF) for the classical modeling and simulation of 2D-periodic Fe_3O_4–organic interfaces. This FF combination features improved electrostatic description through a QM-based per-layer rescaling protocol of the original CLAY-based partial atomic charges[48] originally derived for bulk materials. Nevertheless, to the best of our knowledge, there is still a lack of systematic computational studies assessing and benchmarking the transferability of mCLAY FF parameters in the description of zero-dimensional Fe_3O_4–based materials (e.g., nanoparticles) and expanding their applicability across a broader range of biomolecular FF frameworks.

In this work, we present a computational protocol for an effective classical modeling and simulation of zero-dimensional organic-coated Fe_3O_4 nanoparticles (NPs) of realistic size, validated in a bottom-up fashion against higher-level QM data, which still stand a challenging task in this computational niche. The aim is to design Fe_3O_4 NP structures for applications in modeling more complex nanosystems interfacing molecular assemblies of simple organic composition (consisting of H, C, O, and N atoms), expanding the applicability of mCLAY FF within the CHARMM FF framework for biomolecular components. To achieve this, we first rescale CLAY-based partial atomic charges to describe 2D-periodic pristine Distorted Bulk Truncated (DBT) Fe_3O_4 (001) surfaces using the protocol proposed in ref. 39. Additionally, we evaluate the combination of the mCLAY FF with the mainstream biomolecular CHARMM FF in classically describing 2D-periodic organic-coated DBT Fe_3O_4 (001) slabs. Moving ahead, we fully characterize a zero-dimensional pristine 2.3 nm Fe_3O_4 NP, ensuring the transferability of this set of FF parameters in describing larger NP structures beyond the reach of full QM characterizations. Next, we propose a computational protocol for the classical modeling of an organic-coated 5 nm Fe_3O_4 NP, providing an accurate nanostructure support for further polymeric coating. Finally, we investigate the influence of different PEG chain lengths, coated in a homogeneous or heterogeneous manner onto the Fe_3O_4 NP surface, on key quantities such as polymer coating thickness, chain's order parameters, and H-bond formation within the polymer corona, highlighting the strengths and limitations of the proposed computational protocol in describing such complex bio-inorganic assemblies.

Results

The results are presented as follows: in Section "Preparation of Structural Models", we provide all the details on the preparation of the slab and nanoparticle models. In Section "Pristine DBT Fe_3O_4 (001) slab", we present the protocol adopted for estimating the per-layer CLAY-based partial atomic charges for Fe and O atoms within the 2D-periodic pristine DBT Fe_3O_4 (001) slab. In Section "Fully Formate-Coated DBT Fe_3O_4 (001) slab", we assess the accuracy of the derived partial atomic charges combined with the mCLAY/CHARMM FF in describing a 2D-periodic FA-coated DBT Fe_3O_4 (001) slab compared to their QM counterpart predictions using DFTB MD simulations. In Section "Pristine Fe_3O_4 Nanoparticles: Exploring Small and Large Structures" we proceed by characterizing small (2.3 nm) and large (5.0 nm) Fe_3O_4 NP structures using DFT/HSE06 and DFTB calculations to validate the transferability of the mCLAY FF in describing these zero-dimensional materials. In Section "Coating Realistic-size 5 nm Fe_3O_4 Nanoparticles", we propose a systematic computational protocol for accurately modeling starting-point structures of realistic-size polymer-coated 5.0 nm Fe_3O_4 nanosystems with varying coating compositions. In Section "Anchoring Group Binding and Stability on 5 nm Fe_3O_4 Nanoparticles in Solution", we evaluate the ability of the implemented FF to describe potential transitions in the binding configuration of anchoring groups on the NP surface of these polymer-coated Fe_3O_4 nanosystems in physiological solution. In Section "Case Study of NH_3^+-terminated PEG-coated 5 nm Fe_3O_4 Nanoparticles in Aqueous Solution: The impact of non-Homogeneous Length of Polymer Chains", we conduct an in-depth investigation into the effects of homogeneous and heterogeneous coating strategies on key parameters of the polymer-coated Fe_3O_4 nanosystems in physiological solution. This includes discussions on key aspects for designing tailored nanosystems for nanomedical applications, such as *Coating Thickness and Radius of Gyration*, *Order Parameter of PEG chains*, and *Polymer Corona H-bonding analysis*. Throughout the manuscript, mean and plus and minus standard deviation (σ) are reported as mean $\pm\,\sigma$.

Preparation of structural models

Pristine DBT Fe_3O_4 (001) slabs. The DBT surface model[49] was used to model pristine DBT Fe_3O_4 (001) surfaces and it was constructed as a (1×1) 17-layer slab with inversion symmetry, in line with previous work by some of us[36,37,50–52]. In the DFT/HSE06 optimization calculations, the atoms in the central five layers of the slab were kept fixed to their bulk positions, whereas the atoms in the other layers were fully relaxed. In the DFTB optimization calculations and DFTB MD simulations, all the atoms were fully relaxed. At classical level of theory, the pristine Fe_3O_4 slab in vacuum was classically modeled using the same (1×1) 17-layer DBT surface model as in the QM calculations, where all the atoms were fully relaxed during energy minimization and MD simulations.

Formate-coated DBT Fe_3O_4 (001) slabs. A full coverage regime of formate was modeled by saturating all under-coordinated octahedral Fe sites on both surfaces of the DBT Fe_3O_4 (001) slab with two bidentate dissociated formic acid molecules. At the QM level, only DFTB optimization calculations and DFTB MD simulations were performed. At classical level of theory, the fully formate-coated DBT Fe_3O_4 (001) surface in vacuum was modeled by placing two dissociated formic acid molecules on each side of the slab, as done in the DFTB calculations. A larger fully formate-coated Fe_3O_4 (001) surface was also classically modeled by replicating the unit cell three times (3×3) in both the x and y directions. In both (1×1) and (3×3) fully formate-coated DBT Fe_3O_4 (001) slab models, all the atoms were fully relaxed during the energy minimization and MD simulations.

Pristine and coated Fe_3O_4 nanoparticles. The 2.3 nm NP model used in this investigation is enclosed by six DBT (001) facets, as observed in previous experiments[9,11]. It consists of 1466 atoms with edge length of ca 2.3 nm (i.e., 2.75 times the bulk magnetite lattice parameter) and was obtained from the one proposed by Liu and Di Valentin[37] with corners reconstruction in a bulk-truncated fashion. The total magnetization can be computed according to the formula in Eq. 1, which determines the total magnetic moment of a magnetite system, as proven in ref. 37:

$$m_{tot} = 5 \times \left[N\left(Fe^{3+}_{Oct}\right) - N\left(Fe^{3+}_{Tet}\right)\right] + 4 \times \left[N\left(Fe^{2+}_{Oct}\right) - N\left(Fe^{2+}_{Tet}\right)\right] \quad (1)$$

where Fe^{3+}_{Oct} and Fe^{2+}_{Oct} are the ions at octahedral sites, Fe^{3+}_{Tet} and Fe^{2+}_{Tet} are the ions at tetrahedral sites, and N is the number of the corresponding ions. Similar to what occurs in bulk magnetite, for and the high-spin $3d^5$ configuration gives an atomic magnetic moment of $+5$ and -5 μ_B, respectively whereas the high-spin $3d^6$ electron configuration gives $+4$ and -4 μ_B, respectively.

The cubic Fe_3O_4 NP model of ca 5 nm (11897 atoms with edge length of ca 4.9 nm, 5.75 times the bulk magnetite lattice parameter) was obtained by cutting bulk magnetite along the (001) planes following the same protocol as outlined for the smaller 2.3 nm Fe_3O_4 NP model[37]. This larger Fe_3O_4 NP model is also enclosed by six DBT (001) facets and presents the same type of corners and edges as those of the smaller NP. This 5 nm Fe_3O_4 NP was then fully coated with zwitterionic carbamate (from now on CA) ligands, accounting in total 432 ligands (72 ligands per NP facet), whose carboxylate groups were equally adsorbed over all pairs of undercoordinated Fe sites exposed on the NP surface using in-house scripting via the MOLTEMPLATE program[53], resulting in a grafting density at the theoretical limit of ~2.9 ligand/nm^2. This corresponds to the scenario in which every pair of undercoordinated octahedral Fe sites on the Fe_3O_4 nanoparticle surface has one carboxylate group adsorbed in a bridging bidentate mode. The grafting density adopted in our models aligns well with the experimental findings by

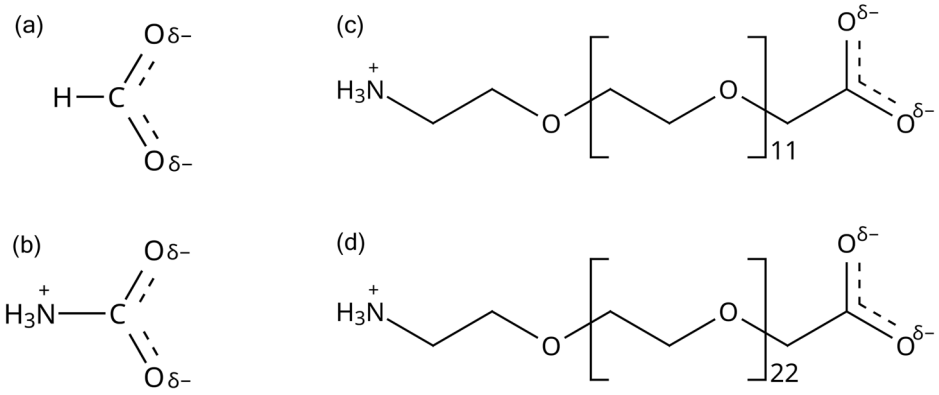

Fig. 1 | Chemical structures of small organic ligands and polymeric chains. 2D molecular representations of the coating molecules studied herein: **a** Formate ion, **b** Carbamate ion, **c** PEG_{500}-NH_3^+ and **d** PEG_{1k}–NH_3^+ polymeric chains.

Amstad et al.[54] *using the grafting–to* method, who achieved a grafting density up to 2.5–2.8 ligand/nm^2 of PEG_{5k} chains, assessed respectively by XPS and TGA analysis, for Fe_3O_4 NPs with a similar diameter (6 ± 1 nm). The authors also reported that ligands were irreversibly adsorbed onto the IONPs surface through the formation of stable bridging bidentate complexes between the ligand's oxygen atoms and their corresponding anchoring iron sites. This model underwent classical energy minimization in vacuum using the Polak-Ribieri version of the conjugated gradient using a stopping tolerance for force equal to 1.0e^{-6}. The resulting classically optimized CA-coated 5.0 nm Fe_3O_4 NP structure was benchmarked for both overall NP thickness and interatomic distance between the carboxylate oxygen atoms of CA ligands and their corresponding anchoring Fe sites on the NP surface against higher-level QM-derived reference data. After validation, this optimized CA-coated NP structure was subjected to further modification, in which the capping –**NH$_3^+$** groups of CAs were removed, while their adsorbed -**COO$^-$** groups (with an open valence in the carbon atom) were kept at their optimized geometry on the NP surface. The methylene group of the -**C**H$_2$-PEG$_X$-NH$_3^+$ chain (with an open valence in the first carbon atom) was positioned at an optimal distance from the carbon atom of -**C**OO$^-$ groups using in-house scripting, followed by the assignment of all necessary bonded parameters to covalent bond the two carbon atoms with open valence ($^-$OO**C**-**C**H$_2$-PEG$_X$-NH$_3^+$) according to CGenFF[55–57] (for the sake of simplicity, we interchangeably refer CGenFF as CHARMM FF throughout the manuscript). Three polymer-coated 5 nm Fe_3O_4 nanosystems were built upon this classically optimized CA-coated 5 nm Fe_3O_4 NP structure (Please see Section "Coating Realistic-size 5 nm Fe_3O_4 Nanoparticles" for further details) with three different coating compositions modeled: a homogeneous coating with PEG_{500} chains (HoCo-PEG_{500}), a heterogeneous coating comprising a 50/50 mixture of PEG_{500} and PEG_{1k} (HeCo-$PEG_{500/1k}$), and a homogeneous coating with PEG_{1k} (HoCo-PEG_{1k}).

For all analyses presented in Section "Case Study of NH_3^+-terminated PEG-coated 5 nm Fe_3O_4 Nanoparticles in Aqueous Solution: The impact of non-Homogeneous Length of Polymer Chains", the classically optimized 5 nm Fe_3O_4 NP structure including the bridging bidentate binding configuration of the carboxylate anchoring groups on the Fe_3O_4 NP surface (as supported by both DFT calculations and experiments conducted in vacuum) was treated as an independent and thermalized structure at 303.15 K free to undergo translation and rotation during the MD simulations, following similar protocol utilized by some of us in previous work [58,59]. This rigid restraint of anchoring groups also ensured a constant grafting density across all polymer-coated systems. For the assessment of the mCLAY/CHARMM force field (FF) capabilities in describing the dynamic behavior of the carboxylate anchoring groups under the effects of finite temperature and solvation in the HoCo-PEG_{500}, HeCo-$PEG_{500/1k}$, and HoCo-PEG_{1k} systems (Section "Anchoring Group Binding and Stability on 5 nm Fe_3O_4 Nanoparticles in Solution"), we performed two sets of calculations with different modeling approaches: 1) In the first, the classically optimized Fe_3O_4 nanoparticle was treated as a thermalized rigid body structure, while the rest of the system (anchoring groups, polymer chains, solvent, and ions) evolved freely according to the FF directives, without any rigid restraints (called Rigid NP); 2) In the second setup, the entire system was allowed to evolve freely over time, governed solely by the FF directives (called All Relaxed). Each of the three systems (HoCo-PEG_{500}, HeCo-$PEG_{500/1k}$, and HoCo-PEG_{1k}) was simulated under both modeling setups. The simulation boxes were filled with the rigid mTIP3P water model[60] at the experimental density of 0.99 g/cm^3 ensuring a minimum buffer distance of 20 Å between the NP and the box edges, setting the salt concentration of the solution at 0.15 M using its respective ad hoc parametrized Na^+ and Cl^- ions[61,62]. The Ligand Reader & Modeler module in the CHARMM-GUI webserver[63,64] was utilized to build up the three-dimensional structures of PEG_{500}-NH_3^+ and PEG_{1k}-NH_3^+ chains and bonded and non-bonded parameters were assigned using the CGenFF. All the organic ligands and polymer coating molecules studied herein are compiled in Fig. 1.

Pristine DBT Fe_3O_4 (001) flat surface

We begin by adopting the same approach proposed in ref. 39 to rescale CLAY-based partial atomic charges for pristine and organic-coated sub-surface cation vacancy (SCV) and DBT Fe_3O_4 surfaces in vacuum. However, it is worth noting some differences compared to our approach: I) To derive rescaled CLAY-based partial atomic charges for iron and oxygen atoms in bulk or slab Fe_3O_4 models, we rely on the charge analysis using HSE06 hybrid functionals (DFT/HSE06) in CRYSTAL17 (Mulliken analysis); II) we not only differentiate the iron atoms with different coordination numbers, but we also distinguish the iron atoms accordingly to their respective oxidation state – the Fe^{3+} and Fe^{2+} partial atomic charges are assigned according to the Fe^{3+}/Fe^{2+} disproportion estimated by the DFT/HSE06 calculations. We rescale the original CLAY-based partial atomic charges according to Eq. (2):

$$q^{FF}_{layer}(ion) = q^{FF}_{bulk}(ion) \cdot \frac{\left\langle q^{DFT}_{layer}(ion) \right\rangle}{\left\langle q^{DFT}_{bulk}(ion) \right\rangle} \tag{2}$$

where $q^{FF}_{layer}(ion)$ stands for the re-scaled FF point-charge for each specific atomic species in their corresponding DBT Fe_3O_4 layers; $q^{FF}_{bulk}(ion)$ stands for the FF point-charge for each specific bulk atomic species; $\left\langle q^{DFT}_{layer}(ion) \right\rangle$ represents the average of DFT/HSE06 point-charge values derived for each specific atomic species within either the surface or sub-surface Fe_3O_4 layer; and $\left\langle q^{DFT}_{bulk}(ion) \right\rangle$ represents the average DFT/HSE06 point-charge values derived for each specific atomic species within the bulk Fe_3O_4 region.

Table 1 reports the q^{DFT}_{layer} and q^{FF}_{layer} for all Fe_3O_4 atomic species (please also see Supplementary Table 1 for q^{DFT}_{bulk} and q^{FF}_{bulk}) – the calculated partial atomic charge model is broken down into three main atomic layers, namely, bulk, sub-surface, and surface Fe_3O_4 atoms in which all these atoms are differentiated according to their respective oxidation state Fe^{3+}_{Tet}, Fe^{3+}_{Oct}, Fe^{2+}_{Oct} at their corresponding layer.

After rescaling the DFT/HSE06 partial atomic charges using Eq. (2), we standardize the partial atomic charges for Fe_3O_4 atoms sharing the same oxidation state within the subsurface and the bulk layers. We do so by adjusting these charges to align with the ones found in the bulk region, as we see no significant differences in their values compared to the bulk CLAY-based partial atomic charges. These adjusted DFT/HSE06 partial atomic charges are then multiplied by their corresponding number of atoms within each layer of the pristine DBT Fe_3O_4 surface slab, resulting in a net positive charge of +1.408. To ensure overall electroneutrality, we further refine the charge values within the surface layer by redistributing the excess positive charge among the oxygen atoms in the first layer (O_1) until they reach an integer number - the remaining residual positive charge is then adjusted by scaling down the partial atomic charges of Fe^{3+}_{Tet1} and Fe^{3+}_{Oct1} until a zero net charge is achieved.

Table 1 | Rescaled CLAY-based partial atomic charges for each atomic species in the pristine DBT Fe_3O_4 (001) surface model derived from Eq. (2)

Atom type	# of atoms	q^{DFT}_{layer} charges	Rescaled q^{FF}_{layer}	Modified q^{FF}_{layer}	Final q^{FF}_{layer}
$Fe^{3+}_{tet_1}$	4	+2.209	+1.592	+1.592	+1.530
$Fe^{3+}_{oct_1}$	8	+2.210	+1.561	+1.561	+1.498
O_1	16	−1.441	−0.959	−0.959	−1.000
Fe^{3+}_{tet2}	4	+2.183	+1.573	+1.574	+1.574
Fe^{3+}_{oct2}	8	+2.230	+1.575	+1.574	+1.574
O_2	16	−1.558	−1.037	−1.050	−1.050
Fe^{3+}_{tet3}	8	+2.187	+1.576	+1.574	+1.574
Fe^{3+}_{oct3}	8	+2.224	+1.571	+1.574	+1.574
Fe^{2+}_{oct3}	12	+1.890	+1.049	+1.052	+1.052
O_3	40	−1.577	−1.050	−1.050	−1.050
System Net Charge		−0.008	+1.576	+1.408	0.000

For clarity, atoms are distinguished by their coordination sites and their layer position in the slab. Atom counts are also given for each of these idealized layers in the normal direction of the DBT Fe_3O_4 (001) slab. The subscript number in the first column refers to (1) surface atoms, (2) sub-surface atoms, and (3) bulk atoms in the Fe_3O_4 slab.

It is also noteworthy to mention the similarity in the final set of partial atomic charges implemented in the mCLAY FF for describing the classical atoms on the pristine DBT Fe_3O_4 (001) surface, despite utilizing a different DFT approach compared to Konuk et al.[39] For instance, they reported partial atomic charges of +1.461 *e*, +1.589 *e* and −1.000 *e* for the Fe_{oct}, Fe_{tet}, and O_1 atoms in their set of force field parameters, respectively. In comparison, our protocol yielded partial atomic charges of +1.498 *e*, +1.530 *e*, and −1.000 *e* for the Fe_{oct}, Fe_{tet}, and O_1 atomic species, respectively.

Fully formate-coated DBT Fe_3O_4 (001) flat surface

An important step here is to ensure the suitability of rescaled CLAY-based partial atomic charges (and their respective mCLAY LJ (12-6) parameters) in combination with the CHARMM FF for describing the adsorption process of organic molecules of simple composition (H, C, O, N) on the DBT Fe_3O_4 (001) surface. So, we begin by studying the adsorption of dissociated formic acid onto the pristine DBT Fe_3O_4 (001) surface.

There are two main reasons for starting from this simple model: I) the carboxylate group as in dissociated formic acid, i.e. formate ions (FA), is a commonly used anchoring group well known for its ability to establish stable chemical bonds with undercoordinated surface (octahedral) Fe^{3+} atoms on the DBT Fe_3O_4 surface. Modeling such a system is also possible at the DFTB level of theory, which allows us to validate its atomistic counterpart, i.e., Fe-O_{FA} bond distances and Fe_3O_4 slab thickness; II) Similar short organic ions can also serve as a linker molecule, allowing further conjugation with other classes of biomolecules broadening the NP applications. Later in this work, we take advantage of a similar linker molecule for the attachment of biomolecules.

We validate the classical model of the FA-coated Fe_3O_4 (001) slab model at the full coverage regime in vacuum (Fig. 2) by confronting it with its QM counterpart simulated using DFTB MD. FA, each bearing a formal negative charge of −1 *e* each, are placed at the appropriate adsorption iron sites on the DBT Fe_3O_4 (001) surface. Moreover, the protons dissociated from the formic acid molecules are adsorbed on those mostly reactive nearby oxygen atoms on the DBT Fe_3O_4 (001) surface bearing a partial atomic charge of +0.4 *e*.

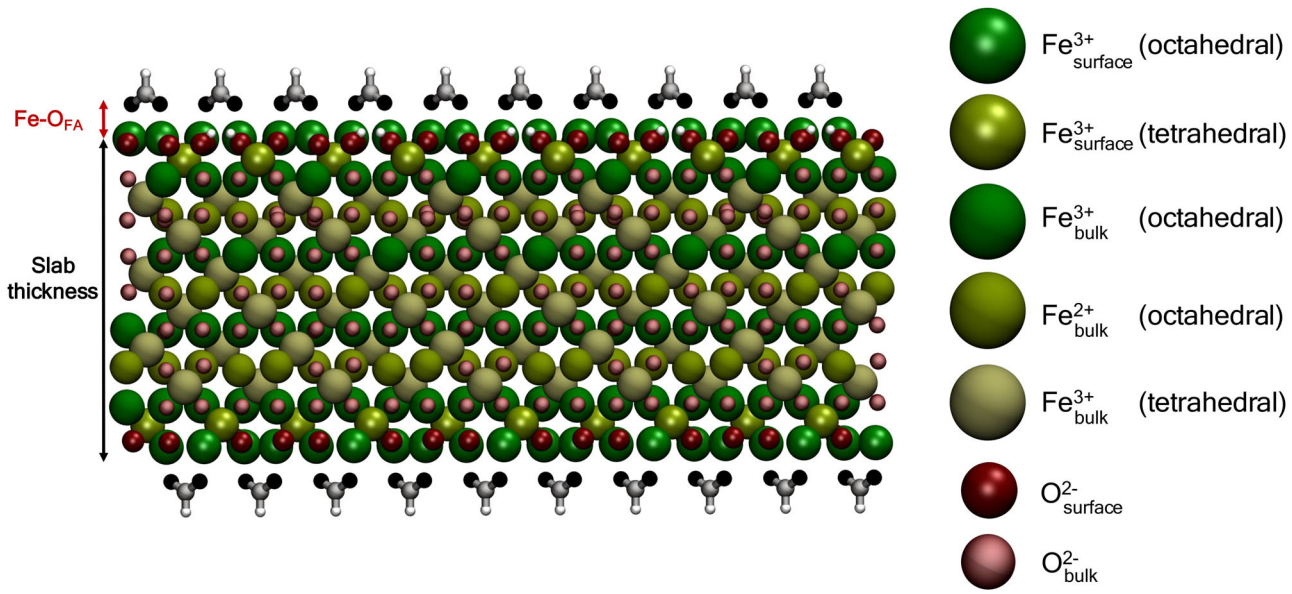

Fig. 2 | Representation of the formate-coated DBT Fe_3O_4 (001) slab at the full coverage regime. Iron and oxygen atoms are color-coded (right-hand side) based on their coordination number and position in the Fe_3O_4 slab, distinguishing surface (shiny colors) and bulk atoms (chalk colors). The adsorbed formate ligand atoms are colored as follows: formate oxygen atoms (black), formate carbon atom (gray), formate and dissociated hydrogen atoms (white).

Compared to the protocol for the assignment of partial atomic charge for the pristine DBT Fe_3O_4 slab system in vacuum, the scenario is somewhat different when dealing with the fully FA-coated Fe_3O_4 slab system in vacuum. This discrepancy arises from the introduction of four dissociated and adsorbed FA molecule on both the upper and lower surface of the DBT Fe_3O_4 (001) slab resulting in an unbalanced net charge for the whole system, if partial atomic charges are those derived for the pristine DBT Fe_3O_4 slab system in vacuum. The imbalance is because the −4 *e* of the four FA is only partially compensated by the four dissociated protons adsorbed on the Fe_3O_4 surface, each bearing a partial atomic charge of +0.4 *e* (for a total of +1.6 *e*). Therefore, there remains an unbalanced excess of −2.4 *e* that requires compensation to ensure the system's electroneutrality. To address this, we start by splitting the DBT Fe_3O_4 slab into two distinct layers, namely the surface and the bulk, following the same protocol outlined previously in Section "Pristine DBT Fe_3O_4 (001) slab". For the bulk region, we assign the same partial atomic charge values derived for the bulk atoms in the pristine DBT Fe_3O_4 slab in vacuum (Table 1). For the re-assignment of partial atomic charges on the surface layer, we test three different forms of charge redistribution for the Fe^{3+}_{Tet1}, Fe^{3+}_{Oct1}, O_1 atoms, as outlined in Table 2. The compilation of bonded and non-bonded mCLAY and CHARMM parameters for modeling the fully FA-coated DBT Fe_3O_4 (001) slab are given in Supplementary Table 2.

To assess how different charge distributions impact the fully FA-coated DBT Fe_3O_4 slab, we conduct a comparative analysis of the overall slab thickness and the Fe-O_{FA} distances from the atomistic MD and DFTB MD simulations. First, we begin by assessing the accuracy of the combination between the mCLAY and CHARMM FFs in describing the Fe-O_{FA} bond distance on the DBT Fe_3O_4 (001) surface, as well as the overall thickness of the Fe_3O_4 (001) slab. We observe that the different strategies for adjusting the CLAY-based partial atomic charges of Fe_3O_4 surface atoms (sets A, B, and C in Table 2) have no significant impact on the average Fe-O_{FA} bond distance and the overall thickness of the Fe_3O_4 (001) slab, as shown in Table 3. Instead, we note that the LJ (12-6) parameter assigned to the FA oxygen atoms is playing a key role in determining the resulting Fe-O_{FA} bond distance. Upon analysis of Table 3, we observe that the original CHARMM LJ (12-6) parameter assigned to the O_{FA} atoms underestimates the Fe-O_{FA} bond distance compared to the reference DFTB MD predictions. However, switching the CHARMM LJ (12-6) parameter of O_{FA} atoms to the original mCLAY LJ (12-6) parameter for oxygen atoms results in an improvement in the Fe-O_{FA} bond distance compared to the DFTB MD reference data while no significant change is noticed in the thickness of the Fe_3O_4 slab. Further comparisons for the Fe-O_{FA}, Fe-O_1, Fe-O_2 distances and overall Fe_3O_4 slab thickness for optimized FA-coated DBT Fe_3O_4 structures at DFT, DFTB, and classical level of theories can be found in Supplementary Note 1 and Supplementary Table 3.

This observation suggests an improved description by the mCLAY FF to describe the short-range interactions between iron and oxygen atoms of FA adsorbed on the surface of the Fe_3O_4 slab when in combination with the CHARMM FF. This modification is justifiable, as the CHARMM-based LJ (12-6) parameters for the oxygen atoms of FA were originally parametrized for a different environment (e.g. aqueous solution), and hence, greater accuracy compared to the QM predictions should be expected by the mCLAY-FF description of these FA oxygen atoms in a non-solvated environment interfacing the Fe_3O_4 (001) surface atoms.

Lastly, to check the potential influence of system size on the Fe-O_{FA} bond distance and the thickness of the Fe_3O_4 slab, we replicate the unit cell of the fully FA-coated Fe_3O_4 slab into a 3×3 model and we repeat the same simulations and analysis as done for the smaller 1×1 system, and no significant differences are observed (Supplementary Table 4).

Overall, we confirm reasonable agreement between atomistic and DFTB MD predictions for both the Fe-O_{FA} bond distance and the thickness of the (FA-coated) Fe_3O_4 slab in vacuum using the per-layer point charge model and the mCLAY/CHARMM FF combination. Moving ahead, we proceed benchmarking the transferability of this set of FF parameters, so far validated for the atomistic description of pristine and organic-coated 2D Fe_3O_4 systems, for the description of classically zero-dimensional cubic-shaped Fe_3O_4 materials as well.

Table 2 | Rescaled mCLAY- and CHARMM-based partial atomic charges for each atomic species in the DBT Fe_3O_4 (001) slab model and the dissociated formic acid, respectively

Atom type	# of atoms	Adjusted partial atomic charges A|B|C
Fe^{3+}_{tet1}	4	+1.630|+1.730|+1.530
Fe^{3+}_{oct1}	8	+1.698|+1.698|+1.598
O_1	16	−0.975|−1.000|−0.900
Fe^{3+}_{tet2}	12	+1.574
Fe^{3+}_{oct2}	16	+1.574
Fe^{2+}_{oct2}	12	+1.052
O_2	56	−1.050
Total Charge of the Fe_3O_4 Slab		+2.400
H_o	4	+0.400
Total charge of the adsorbed proton ion		+1.600
O_{FA}	8	−0.760
C_{FA}	4	+0.520
H_{FA}	4	+0.000
Total Net Charge of Formate ions		−4.000
System Net Charge		0.000

For clarity, atoms are distinguished by their coordination sites and their layer position in the slab. Atom counts are also given for each of these idealized layers in the normal direction of the DBT Fe_3O_4 (001) slab.

Pristine Fe_3O_4 nanoparticles: exploring small and large structures

We begin by characterizing a 2.3 nm cubic Fe_3O_4 enclosed by six (001) facets at DFT/HSE06 and DFTB levels of theory. Since this system can be fully characterized at these two QM levels of theory, it will serve as the reference model for the assessment of FF transferability to describe this zero-dimensional material.

Through DFT/HSE06 calculations, we initially identify and enumerate each atomic species in the pristine 2.3 nm Fe_3O_4 NP structure, as shown in Table 4. Subsequently, we assign the CLAY-based partial atomic charges following the same protocol adopted for the pristine DBT Fe_3O_4 (001) slab in Section "Pristine DBT Fe_3O_4 (001) slab". Specifically, we split the atoms of

Table 3 | Average Fe-O_{FA} bond distances on the (1×1) DBT Fe_3O_4 (001) surface and overall thickness of the Fe_3O_4 (001) slab estimated from DFTB and atomistic MD simulations at 300 K

Unit (Å)	DFTB[a]	Model A	Model B	Model C	Model A[b]
Fe-O_{FA}	1.99 ± 0.01	1.85 ± 0.01	1.85 ± 0.01	1.86 ± 0.01	1.92 ± 0.02
Thickness	17.7 ± 0.1	17.1 ± 0.3	17.1 ± 0.3	17.3 ± 0.3	17.3 ± 0.3

[a]DFTB 50 ps long MD simulations at 300 K.
[b]mCLAY-based LJ (12-6) parameter for the O_{FA} atoms.

the Fe_3O_4 NP into two regions: an outer region containing only the surface atoms (Fe^{3+}_{Tet1}, Fe^{3+}_{Oct1}, O_1) and an inner region containing the bulk atoms composing the NP core (Fe^{3+}_{Tet2}, Fe^{3+}_{Oct2}, Fe^{2+}_{Oct2}, O_2).

For both the surface layer and bulk region, we begin assigning equivalent rescaled CLAY-based partial atomic charges previously derived for the pristine DBT Fe_3O_4 (001) slab in vacuum (Table 1, Section "Pristine DBT Fe_3O_4 (001) slab"), yielding an unbalanced excess of +0.808 *e* which is then counterbalanced with a total charge of −0.808 *e* evenly spread over all oxygen atoms in the surface layer atoms to ensure the NP's electroneutrality in vacuum.

To assess the mCLAY FF accuracy in describing the pristine 2.3 nm Fe_3O_4 NP in vacuum, we perform both energy minimization and equilibration, followed by 50 ns of MD production in vacuum at classical level and then we compare the obtained thickness with that predicted from its QM counterparts optimized at both DFT/HSE06 and DFTB levels of theory. To quantify the NP thickness, we measure the distance between the geometric center of Fe^{3+} atoms in the octahedral sites on opposite edges of the same facet of the NP and then we average it over all the six NP facets over the 50 ns of production phase. The classical description results in an NP thickness of 23.32 ± 0.19 Å, with a deviation of +3.00% and +0.04% compared to the DFT/HSE06 (NP thickness = 22.64 Å) and DFTB (NP thickness = 23.31 Å) reference data, respectively. It is worth noting that the NP shape and structure remains stable over the entire MD simulation in vacuum.

After confirming the overall stability of the 2.3 nm Fe_3O_4 NP structure over the atomistic MD simulation in vacuum, we move forward by investigating whether the atomic surface layering for the partial atomic charge assignment may affect the NP's overall structure. Here, we evaluate whether suppressing the $Fe^{2+}_{oct2}/Fe^{3+}_{oct2}$ disproportion at the NP core level influences its overall nanostructure. The main idea behind this evaluation is to propose a more general protocol for the assignment of partial atomic charges to larger NP cores, especially when higher-level QM calculations to identify exactly the $Fe^{2+}_{oct2}/Fe^{3+}_{oct2}$ disproportion of the NPs become impractical due to limitations in handling such large systems.

Figure 3 presents two distinct strategies for assigning partial atomic charges in the 2.3 nm Fe_3O_4 NP, using reference QM structural data to assess accuracy in describing the NP structure. In Model A (Fig. 3, left-hand side), we average the partial atomic charges over all Fe^{2+}_{oct2} and Fe^{3+}_{oct2} atoms in the bulk region, as detailed in Supplementary Table 5, Column A. In Model B (Fig. 3, right-hand side), we fully differentiate the atomic species in the second layer, averaging the partial atomic charges over all Fe^{2+}_{oct2} and Fe^{3+}_{oct2} atoms in the bulk region, according to Supplementary Table 5, Column B. The averaging of partial atomic charges follows Eq. (3).

$$q_{FF}\left(Fe^{2+/3+}_{Oct2}\right) = \frac{q\left(Fe^{2+}_{Oct2}\right) \times n\left(Fe^{2+}_{Oct2}\right) + q\left(Fe^{3+}_{Oct2}\right) \times n\left(Fe^{3+}_{Oct2}\right)}{n\left(Fe^{2+}_{Oct2}\right) + n\left(Fe^{3+}_{Oct2}\right)} \quad (3)$$

Then, we perform a 50 ns long MD simulation of both Model A and Model B in vacuum. We find that suppressing the $Fe^{2+}_{Oct2}/Fe^{3+}_{Oct2}$ disproportion at the NP core level yields no difference of the average NP thickness within the standard deviation between Model A (23.31 ± 0.20 Å) and Model B (23.30 ± 0.19 Å). Additionally, we observe no significant difference in the NP thickness compared to the original 2.3 nm Fe_3O_4 NP (23.32 ± 0.19 Å), where there is a fully differentiation of atomic species based on the DFT/HSE06 calculations. When comparing the NP thickness against those predicted by the optimization with DFT/HSE06 (22.64 Å) and DFTB (23.31 Å) calculations, we note that the averaged NP thickness predicted by either classical model is in close agreement with those predicted at both QM levels of theory.

Next, we benchmark a larger pristine 5 nm Fe_3O_4 NP against the lattice parameters of optimized Fe_3O_4 bulk at both DFT/HSE06 and DFTB levels of theory. Since we see no significant deviation in the overall structure of the smaller NP core due to the lack of $Fe^{2+}_{Oct2}/Fe^{3+}_{Oct2}$ disproportion, we follow the protocol adopted for Model A in the partial atomic charge assignment of 5 nm Fe_3O_4 NP atoms (Fig. 3, left-hand side). The NP thicknesses predicted from the lattice parameters of the Fe_3O_4 bulk optimizations at DFT/HSE06 and DFTB levels are 48.24 Å and 48.81 Å, respectively, while the NP

Table 4 | Rescaled CLAY-based partial atomic charges for each atomic species in the pristine 2.3 nm Fe_3O_4 nanoparticle

Atom type	# of atoms	q^{FF}_{layer}	Adjusted q^{FF}_{layer}
Fe^{3+}_{tet1}	76	+1.530	+1.53000000
Fe^{3+}_{oct1}	180	+1.498	+1.49800000
O_1	364	−1.000	−1.00221978
Fe^{3+}_{tet2}	94	+1.574	+1.57400000
Fe^{3+}_{oct2}	174	+1.574	+1.57400000
Fe^{2+}_{oct2}	78	+1.052	+1.05200000
O_2	500	−1.050	−1.05000000
Total System Charge		+0.808	0.00000000

Atoms are categorized by their coordination sites and layer position within the Fe_3O_4 nanoparticle, with the corresponding atom count for each idealized layer.

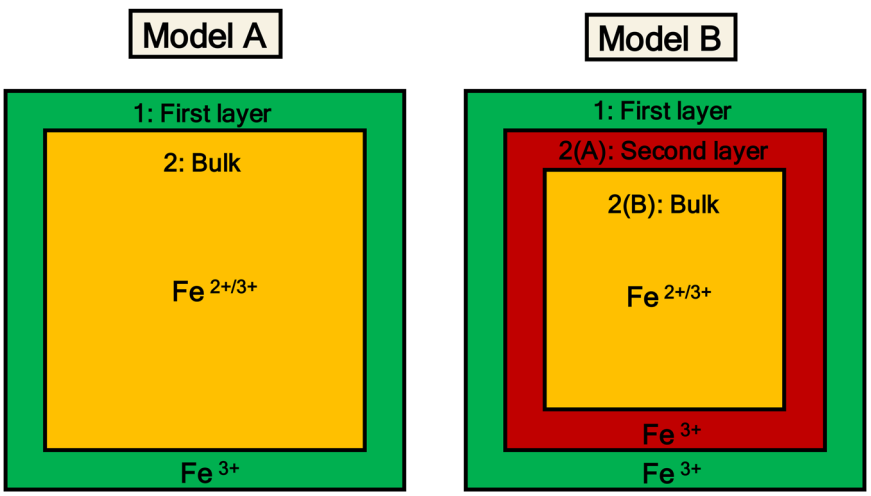

Fig. 3 | Comparative strategies for assigning per-layer partial atomic charges to Fe atoms in Fe_3O_4 nanoparticles. Two distinct approaches for assigning per-layer partial atomic charges to Fe^{2+} and Fe^{3+} atoms in a 2.3 nm Fe_3O_4 (001) nanoparticle are evaluated.

thickness of the classically optimized geometry is 48.77 Å, falling between these two QM values.

At this point, we confirm the reliability of the rescaled point charge model in combination with the mCLAY-FF in providing an accurate and stable structure for the pristine 5 nm Fe_3O_4 NP core. We achieve an excellent compromise between the predictions of the implemented classical model against the overall thickness derived from the lattice parameters of Fe_3O_4 bulk optimization at both DFT/HSE06 and DFTB levels of theory. Now, we are ready to move on to the next step of this work, which involves obtaining an optimized organic-coated 5 nm Fe_3O_4 NP which will undergo slight modifications to serve as the inorganic support of more complex polymer-coated Fe_3O_4 nanosystems.

Coating realistic-size 5 nm Fe_3O_4 nanoparticles

Here, we move towards an important step of this work, which is the modeling of a larger Fe_3O_4 NP structure to serve as inorganic support for polyethylene glycol coatings, one of the aims of this study. Given the prohibitive computational costs, a full QM relaxation of organic-coated 5 nm Fe_3O_4 NPs is not feasible. In such cases, refining classical models using QM reference data becomes challenging due to the large system size, making bottom-up validation unfeasible. However, recalling our findings in previous sections, we can confirm that the synergy between the mCLAY and CHARMM FFs in combination with the rescaled CLAY-based partial point charges is able to accurately catch important aspects of higher-level QM calculations. The thorough characterization and validation of fully FA-coated DBT Fe_3O_4 (001) surfaces against their QM counterparts, along with classical NP thickness predictions for small and large pristine Fe_3O_4 NPs compared to higher-level DFT/HSE06 and DFTB calculations, provide a useful set of reference data that can be translated to larger systems where the QM treatment is prohibitive, such as the distance and orientation of anchoring molecules adsorbed on the Fe_3O_4 (001) surface as well as the overall structure of the inorganic core such as shape and thickness[65,66].

Hence, we propose a step-by-step computational protocol to generate reliable starting-point structures for a large NP structure (5 nm size) to be used as the inorganic core for attachment of PEG chains. In summary, we have four steps in this process: I) cut of the cubic-shaped NP structure from the magnetite bulk and displacement of CHARMM-based zwitterionic carbamate (CA) anchoring molecules with their carboxylate groups on all pairs of octahedral Fe^{3+} sites exposed on the NP surface; II) adjustment of the partial atomic charges of NP atoms ensuring the system's electroneutrality followed by a classical energy minimization of the whole carbamate (CA)-coated NP system in vacuum; III) removal of the capping -NH_3^+ terminal group from the adsorbed CA ligands on the NP surface and IV) formation of the covalent bond between the carbon atom of -**C**OO^- groups adsorbed on the NP surface and the first carbon atom of -**C**H_2-PEG_X-NH_3^+ chains ($^-$OO**C**-**C**H_2-PEG_X-NH_3^+), assigning the proper bonded parameters according to CGenFF. We illustrate all these steps in Fig. 4.

Another important consideration in this approach is the choice of the anchoring ligand used to coat the Fe_3O_4 NP surface, as these groups will serve as the basis for attaching larger biomolecules on it later. Since no QM optimization is feasible for such a large NP core, we aim to retain as much QM information as possible learned from the smaller systems, such as, the average distance between the oxygen atoms of the anchoring groups and their respective adsorption iron sites on the Fe_3O_4 NP surface.

In a scenario where we have used the dissociated form of formic acid, in which each anchoring ion bears a formal negative charge of –1 *e*, a situation of non-electroneutrality arises in the system. Hence, we propose herein the use of the closest organic ligand to FA possessing a zero net charge, namely CA. This anchoring molecule, due to its zwitterionic nature, bears a zero net charge, which ensures the system's electroneutrality in vacuum without substantial modifications of the partial atomic charges in the NP core, while also avoiding artifacts related to the utilization of standard long-range solvers to evaluate electrostatic forces of systems with a non-zero net charge during the classical minimization.

Particular attention has been given to the distance between the oxygen atoms in the carboxylate group of CA and their corresponding adsorption iron sites on the Fe_3O_4 NP surface. We start testing the same set of LJ (12-6) parameters adopted for the FA case, where the CHARMM-based LJ (12-6) parameters for the oxygen atoms in FA are swapped with the ones provided in the mCLAY FF, since the latter perform better in describing the distance between the oxygen atoms in the carboxylate group of FA and their respective adsorption sites on the DBT Fe_3O_4 (001) slab surface. We observe that the mCLAY-based LJ (12-6) parameters overestimate the distance between the oxygen atoms and the iron sites compared to the QM reference. Considering that CHARMM-based LJ (12-6) parameters for the oxygen atoms of carboxylate in CA possess a smaller LJ sigma and similar LJ epsilon values compared to the mCLAY-based ones, we reassign back the former set of LJ (12-6) parameters for the oxygen atoms in CA and perform a classical

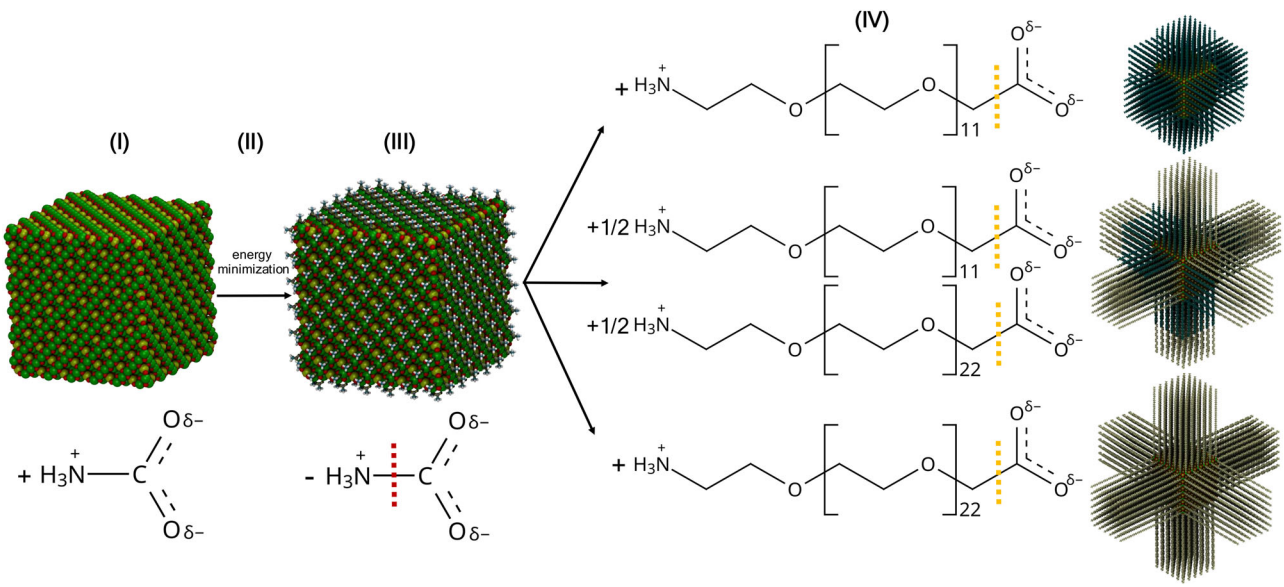

Fig. 4 | Modeling workflow for building up the starting-point structures of the HoCo-PEG$_{500}$, HeCo-PEG$_{500/1k}$, and HoCo-PEG$_{1k}$ nanosystems. Red dashed lines indicate the breakage of covalent bonds in the carbamate ions of the coating, while yellow dashed lines indicate the formation of covalent bonds for the attachment of polymer chains.

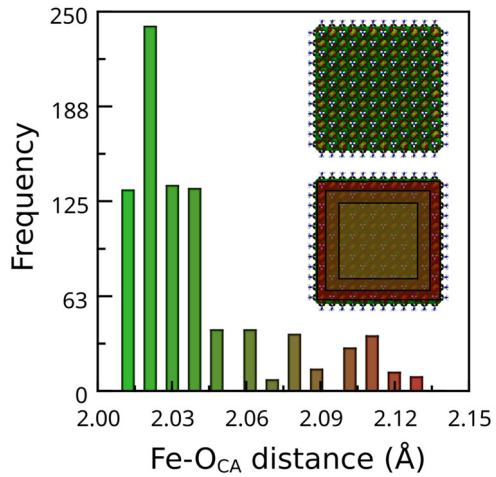

Fig. 5 | Frequency of Fe-O_{CA} distances in the optimized carbamate-coated 5 nm Fe_3O_4 NP structure. The distribution of Fe-O_{CA} is presented, with bar colors corresponding to their respective regions on the DBT (001) NP facets (inset).

energy minimization step to check the average Fe-O_{CA} distances. As expected, we observe an improvement in Fe-O_{CA} distances compared to the DFT/HSE06 and DFTB predictions. The classical prediction of the Fe-O_{CA} distances has an average value of 2.02 Å for the CA ligands over mostly the NP surface and slightly longer (2.10 Å) for the CA ligands on the NP edges. The DFTB and DFT/HSE06 predictions are 1.98–1.99 Å for the Fe-O_{FA} distances on the Fe_3O_4 (001) slab surface, respectively. Figure 5 shows the Fe-O_{CA} distance distributions and their corresponding regions on the DBT Fe_3O_4 (001) NP facets. Moreover, we compile in Table 5 all the necessary bonded and non-bonded FF parameters for the classical optimization of the CA-coated 5 nm Fe_3O_4 NP in vacuum.

With step (IV) of our protocol, we can successfully construct the starting-point structures for the HoCo-PEG_{500}, HeCo-$PEG_{500/1k}$, and HoCo-PEG_{1k} Fe_3O_4 nanosystems. As detailed in Section "Preparation of Structural Models", HoCo-PEG_{500} refers to the homogeneous coating with PEG_{500} chains, HeCo-$PEG_{1k/500}$ refers to the heterogenous coating with a 50/50 mixture of PEG_{1k} and PEG_{500}, and HoCo-PEG_{1k} refers to the homogeneous coating with PEG_{1k} chains. Furthermore, PEG_X-NH_3^+ refers to the positively charged NH_3^+ terminal group of PEG_X chains, where "X" generically represents all PEG chain types when the PEG length is not relevant to the discussion. Since substantial evidence from both DFT calculations (Supplementary Note 2 and Supplementary Table 6) and experiments under ultra-high vacuum conditions[15,67,68] supports the bridging bidentate binding as the most favorable anchoring group configuration, we dedicate the next section to investigate whether this holds true when the nanosystems are immersed in a realistic physiological solution, based on the FF predictions.

Anchoring group binding and stability on 5 nm Fe_3O_4 nanoparticles in solution

Transitions in the binding configurations of anchoring groups, such as carboxylates switching between monodentate and bidentate modes, can occur on organic-coated metal oxide surfaces in solution[69,70]. To evaluate the extent of these conformational transitions at the Fe_3O_4 NP surface at the classical level, we perform two sets of MD simulations using different modeling approaches: 1) In the first, the entire system evolves freely, with no rigid body approximation imposed, relying solely on the FF directives (*All relaxed*); 2) In the second, the rigid body approximation is applied exclusively to the Fe_3O_4 atoms, allowing the rest of the system to evolve according to the FF directives (*Rigid NP*).

Table 6 shows a comparison of the different modeling approaches on the average distance between the carboxylate oxygen atoms and their corresponding Fe anchoring sites on the NP surface (*Fe—O*). It also details the

Table 5 | (a) Combination of partial atomic charges, LJ (12-6) mCLAY and CHARMM FF parameters utilized for the geometry optimization of the carbamate-coated 5 nm Fe_3O_4 NP structure. (b) Set of CHARMM FF parameters for the bonded interactions (bonds, angles, dihedrals, and improper parameters) in carbamate

(a)			
Atom types	ϵ_{ij} **(kcal/mol)**	σ_{ij} **(Å)**	***q* (*e*)**
Fe^{3+}_{tet}	9.0298 (10^{-6})	4.0722	+1.530
Fe^{3+}_{oct}	9.0298(10^{-6})	4.0722	+1.498
O_{surf}	0.1554	3.1655	−1.000
$Fe^{3+}_{tet/bulk}$	9.0298(10^{-6})	4.0722	+1.574
$Fe^{2+/3+}_{oct/bulk}$	9.0298(10^{-6})	4.0722	+1.352
O_{bulk}	0.1554	3.1655	−1.050
H_{car}	0.0460	0.4000	+0.254
C_{car}	0.0700	3.5636	+0.576
N_{car}	0.2000	3.2963	+0.168
O_{car}	0.1200	3.0291	−0.753

(b)				
Bonds	K_b **(kcal/mol)**			b_0 **(Å)**
$C_{car} - N_{car}$	365.0000			1.4200
$C_{car} - O_{car}$	525.0000			1.2600
$N_{car} - H_{car}$	403.0000			1.0400
Angles	K_θ **(kcal/molrad²)**	θ_0 **(°)**	K_{ub} **(kcal/Å²)**	r_{ub} **(Å)**
$C_{car} - N_{car} - H_{car}$	38.0000	112.0000	0.0000	0.0000
$H_{car} - N_{car} - H_{car}$	44.0000	109.5000	0.0000	0.0000
$O_{car} - C_{car} - N_{car}$	40.0000	116.0000	50.0000	2.3530
$O_{car} - C_{car} - O_{car}$	100.0000	128.0000	70.0000	2.2587
Dihedrals	K_χ **(kcal/mol)**	***n***	δ **(°)**	***weightfactor***
$O_{car} - C_{car} - N_{car} - H_{car}$	0.2000	2	180.0000	1.0000
$O_{car} - C_{car} - N_{car} - H_{car}$	0.1500	6	0.0000	0.0000
improper	K_{imp} **(kcal/mol)**			φ_0 **(kcal/mol)**
$C_{car} - O_{car} - O_{car} - N_{car}$	96.0000			0.0000

total number and percentages of anchoring groups that are adsorbed (in either bridging or chelating bidentate configurations or monodentate configurations) or desorbed, out of the total 432 ligands, over the entire production phase across all the six MD simulations.

Our results show that in both modeling approaches, most anchoring groups maintain a bridging bidentate configuration, with only a small fraction transitioning to the monodentate mode and an even smaller fraction acquiring a chelating bidentate configuration or fully desorbing from the Fe_3O_4 NP surface (Table 6). When the rigid body approximation is imposed on the NP core, the average *Fe—O* distance in bidentate anchoring groups slightly increases by approximately 0.10 Å. Furthermore, anchoring groups that transition to the monodentate configuration display similar average *Fe—O* distances for the desorbing oxygen atom.

Regarding the total number of anchoring groups that maintain the bridging bidentate configuration or transition to a chelating bidentate or monodentate configuration during the production phase, we find that imposing the rigid body approximation at the NP core level retains a higher number of these anchoring groups in the bridging bidentate configuration. Furthermore, complete desorption of anchoring groups is minimal and occurs in only a tiny fraction of the ligands, regardless of the modeling approach adopted.

Table 6 | Average distances of oxygen atoms in carboxylate anchoring groups to their corresponding adsorption Fe sites on the 5 nm Fe_3O_4 nanoparticle surface, categorized by their binding mode configuration (bridging or chelating bidentate configurations, or monodentate configuration) and the average number of adsorbed or desorbed anchoring groups for the HoCo-PEG_{500}, HeCo-$PEG_{1k\text{-}500}$, and HoCo-PEG_{1k} nanosystems

(a)			
All relaxed	***HoCo-PEG_{500}***	***HeCo-$PEG_{1k/500}$***	***HoCo-PEG_{1k}***
Fe—O (bridging)[a]	*2.01 ± 0.07*	*2.01 ± 0.07*	*2.01 ± 0.07*
Fe—O (chelating)[a]	*2.06 ± 0.07*	*2.07 ± 0.06*	*2.07 ± 0.07*
Fe—O (monodentate)[a]	*2.86 ± 0.91*	*2.83 ± 0.88*	*2.83 ± 0.88*
Bridging bidentate[b]	*333 ± 13 (77.08%)*	*331 ± 12 (76.62%)*	*319 ± 17 (73.84%)*
Chelating bidentate[b]	*5 ± 2 (1.15%)*	*7 ± 1 (1.62%)*	*6 ± 3 (1.39%)*
Monodentate[b]	*88 ± 10 (20.37%)*	*87 ± 10 (20.14%)*	*101 ± 13 (23.38%)*
Desorbed[b]	*6 ± 2 (1.40%)*	*7 ± 2 (1.62%)*	*6 ± 2 (1.39%)*
(b)			
Rigid NP	***HoCo-PEG_{500}***	***HeCo-$PEG_{1k/500}$***	***HoCo-PEG_{1k}***
Fe—O (bridging)[a]	*2.10 ± 0.07*	*2.10 ± 0.07*	*2.09 ± 0.07*
Fe—O (chelating)[a]	*2.12 ± 0.07*	*2.14 ± 0.07*	*2.13 ± 0.06*
Fe—O (monodentate)[a]	*2.84 ± 0.90*	*2.79 ± 0.85*	*2.81 ± 0.86*
Bridging bidentate[b]	*376 ± 8 (87.04%)*	*372 ± 12 (86.11%)*	*354 ± 14 (81.94%)*
Chelating bidentate[b]	*1 ± 1 (0.23%)*	*1 ± 1 (0.23%)*	*2 ± 1 (0.46%)*
monodentate[b]	*52 ± 6 (12.04%)*	*57 ± 11 (13.20%)*	*74 ± 14 (17.14%)*
desorbed[b]	*3 ± 1 (0.69%)*	*2 ± 1 (0.46%)*	*2 ± 1 (0.46%)*

[a]For the bridging and chelating bidentate configurations, the average Fe—O distance is taken from both adsorbed oxygen atoms in the carboxylate anchoring group, while for the monodentate configuration, the reported averages correspond only to the Fe—O distances of desorbed carboxylate oxygen atoms.
[b]The average number of adsorbed or desorbed anchoring groups is taken over the 50 ns MD production run.

In summary, our findings suggest that the bridging bidentate configuration is the preferred binding mode for carboxylate anchoring groups on the Fe_3O_4 NP surface, with a modest number transitioning to a monodentate configuration and a minimal fraction acquiring a chelating bidentate configuration or undergoing complete desorption, even in the presence of solvent and ions.

Experimental evidence confirms that the oxygen in anchoring groups forms highly stable and irreversible Fe—O bonds on the Fe_3O_4 NP surface under physiological conditions[54,71]. This stability is likely enhanced by the reduced water content near the surface of polymer-coated NPs, favoring the bridging bidentate configuration of carboxylate groups by minimizing competition for Fe binding sites. Therefore, we opt to apply the rigid approximation to both the Fe_3O_4 NP core and the anchoring groups, fixing the latter in the bridging bidentate configuration at their optimized distances obtained with CA ligands (as detailed in Sections "Preparation of Structural Models" and "Coating Realistic-size 5 nm Fe_3O_4 Nanoparticles"). This choice is further supported by DFT calculations (Supplementary Note 2 and Supplementary Table 6) and experimental studies in ultra-high vacuum conditions[15,67,68], which identify the bridging bidentate as the most stable anchoring group configuration on the DBT Fe_3O_4 (001) surface. The use of this approximation also aligns with our understanding that the implemented FF still requires further validation on its capability to quantitatively predict binding configurations and their transitions in realistic solution conditions, making the use of the stable bridging bidentate configuration across all polymer-coated NP models a reasonable approach for this study.

Case study of NH_3^+-terminated PEG-coated 5 nm Fe_3O_4 nanoparticles in aqueous solution: the impact of non-homogeneous length of polymer chains

This final section focuses on investigating the applicability of the HoCo-PEG_{500}, HeCo-$PEG_{500/1k}$, and HoCo-PEG_{1k} nanosystems for quantifying properties that hold significant potential in the design of tailored nanosystems for nanomedical applications. Experimental findings indicate that the polymer length and coating composition of PEGylated Fe_3O_4 NPs are critical parameters for controlling their magnetization properties, polymer structure, and colloidal stability[19,24,72]. Additionally, the chemical nature of the terminal groups of these chains, such as amine groups, plays a key role in facilitating functionalization and conjugation with bioactive molecules[26–28].

In the following, we analyze the impact of different PEG coating compositions on key properties of the polymeric corona surrounding the NP core.

Figure 6 illustrates the final snapshot of the simulated Fe_3O_4 nanosystems with the following coating compositions: (a) HoCo-PEG_{500},(b) HeCo-$PEG_{1k/500}$, and (c)HoCo-PEG_{1k} in physiological solution after a 100 ns long MD production phase.

Coating thickness and radius of gyration. The control of polymeric coating thickness (e.g. polymer chain length) is fundamental for tailoring nanosystem properties to enhance their functionality and performance, for instance, in preventing or controlling the formation of the protein corona[73,74], modulating the presentation of bioactive molecules on the NP surface[22,75], and so forth. Another important aspect of polymer coating is how the coating composition (e.g. heterogeneous or homogeneous coating) may impact the molecular conformation of these polymeric chains within the polymer corona.

Although the polymeric coating thickness can be accurately measured experimentally[76], it is often difficult for experimentalists to understand the intricate interactions behind it at molecular level. Hence, we provide further understanding on how the overall polymeric thickness is impacted by the three different polymer coating compositions.

To do so, we begin by estimating the PEG thickness from the calculation of the number density of PEG particles radially distributed around the NP core having its geometric center as reference. The coating thickness is defined here as the difference between the minimum $r_{\min}$ and maximum $r_{\max}$ distances from the NP surface according to Eq. (4), where $g_{coat}(r_{\min}) = 0.05$ and $g_{coat}(r_{\max}) = 0.95$, therefore corresponding to 90% of probability in finding the polymeric coating particles in that region over the simulation time[77].

$$g_{coat}(r) = \frac{4\pi}{N_{coat}^2}\int_0^r \sum_{i=1}^{N_{coat}} \langle \delta_D(r_i - r') \rangle dr' \tag{4}$$

Yet an important aspect from an experimental point of view is the quantification of the Radius of Gyration (RoG) of polymeric chains in the polymer corona, which is a common characterization in polymer physics[78] and routinely assessed by MD simulations. At its core, this analysis provides useful information about the spatial extent of the polymer coating molecules and contributes to a better understanding of the conformational behavior and flexibility of these molecules in solution and can be given by Eq. (5).

$$R_{gyr}^2 = \frac{1}{M}\sum_{i=1}^{N} m_i (r_i - R)^2 \tag{5}$$

In this section, we unveil the impact of diverse coating morphologies on the PEG coating thickness and RoG of polymer ligands decorating the Fe_3O_4 NP. Figure 7 shows the average values of PEG corona thickness and the RoG for all three systems depicted in Fig. 6.

Figure 7 reveals a significant increase in PEG coating thickness when transitioning from HoCo-PEG_{500} to HeCo-$PEG_{1k/500}$. We also see an increase in thickness when shifting from HeCo-$PEG_{1k/500}$ to HoCo-PEG_{1k},

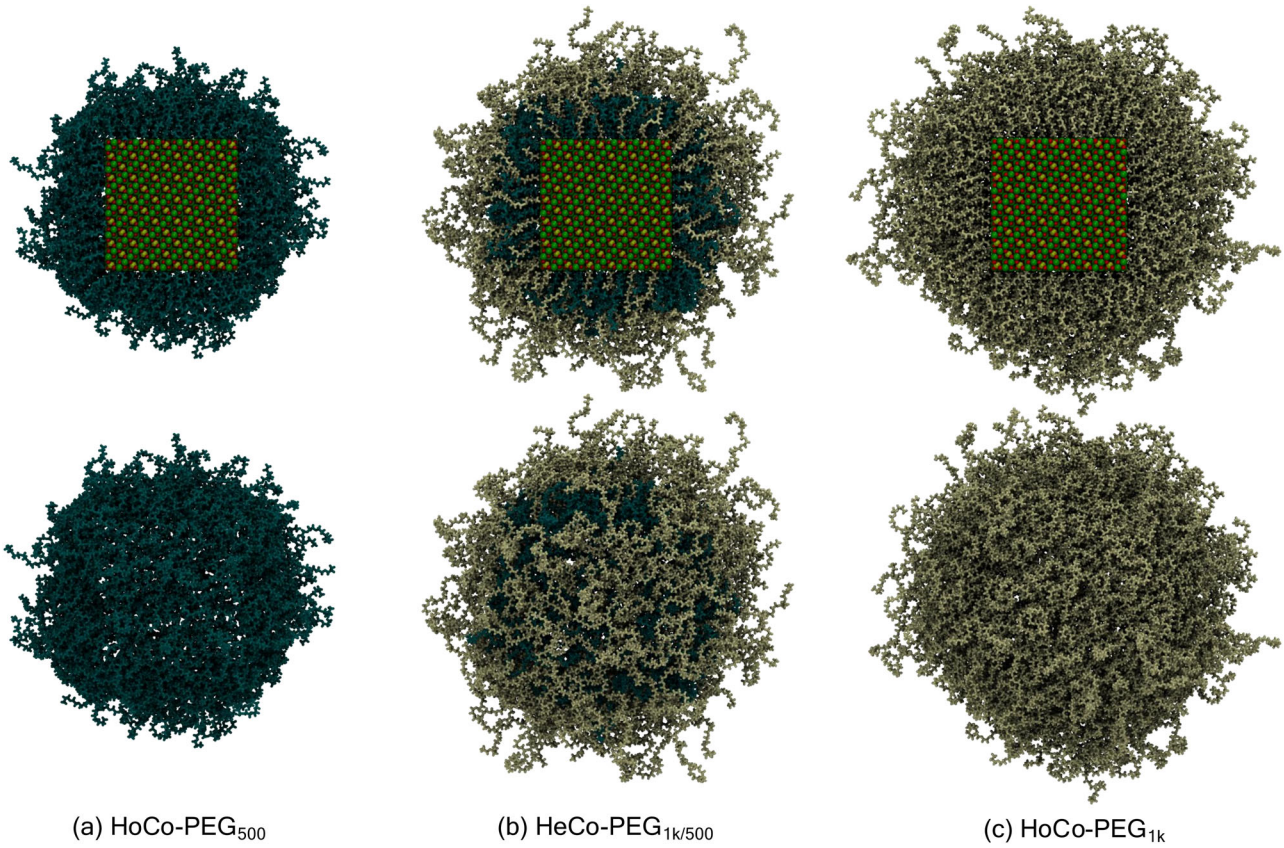

Fig. 6 | Fe_3O_4 nanosystems with varying PEG coating morphologies. Final snapshots of simulated 5 nm Fe_3O_4 nanoparticles with different polymer coatings featuring: **a** homogeneous PEG_{500} coating, **b** heterogeneous $PEG_{1k/500}$ coating with 50/50 mixture of PEG_{500} and PEG_{1k} chains, and **c** homogeneous PEG_{1k} coating.

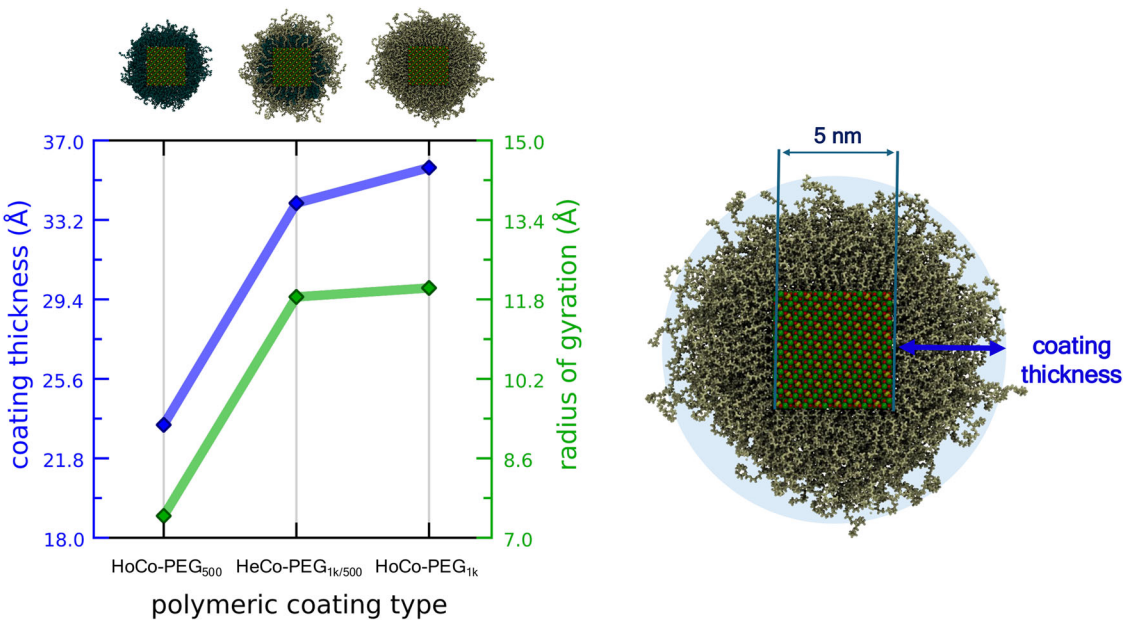

Fig. 7 | Coating thickness and radius of gyration across different PEG coating morphologies. Comparison of coating thickness and radius of gyration for Fe_3O_4 nanoparticles with HoCo-PEG_{500}, HeCo-$PEG_{1k/500}$, and HoCo-PEG_{1k} coatings, highlighting the structural differences across the three different morphologies. Only the RoG of PEG_{1k} chains is plotted for HeCo-$PEG_{1k/500}$, while the RoG of PEG_{500} chains is given in the text.

though to a lesser extent. This suggests that the presentation of PEG_{1k}-NH_3^+ chains towards the bulk-water phase behaves similarly in both cases, where most of these chains acquire a brush conformation towards the bulk-water phase.

Upon analyzing the RoG values of PEG_{500}-NH_3^+ chains across the HoCo-PEG_{500} and HeCo-$PEG_{1k/500}$ coating morphologies, we find distinct effects on their conformational behavior. HeCo-$PEG_{1k/500}$ coating reduces the RoG of PEG_{500}-NH_3^+ chains (6.65 Å) compared to the identical polymer

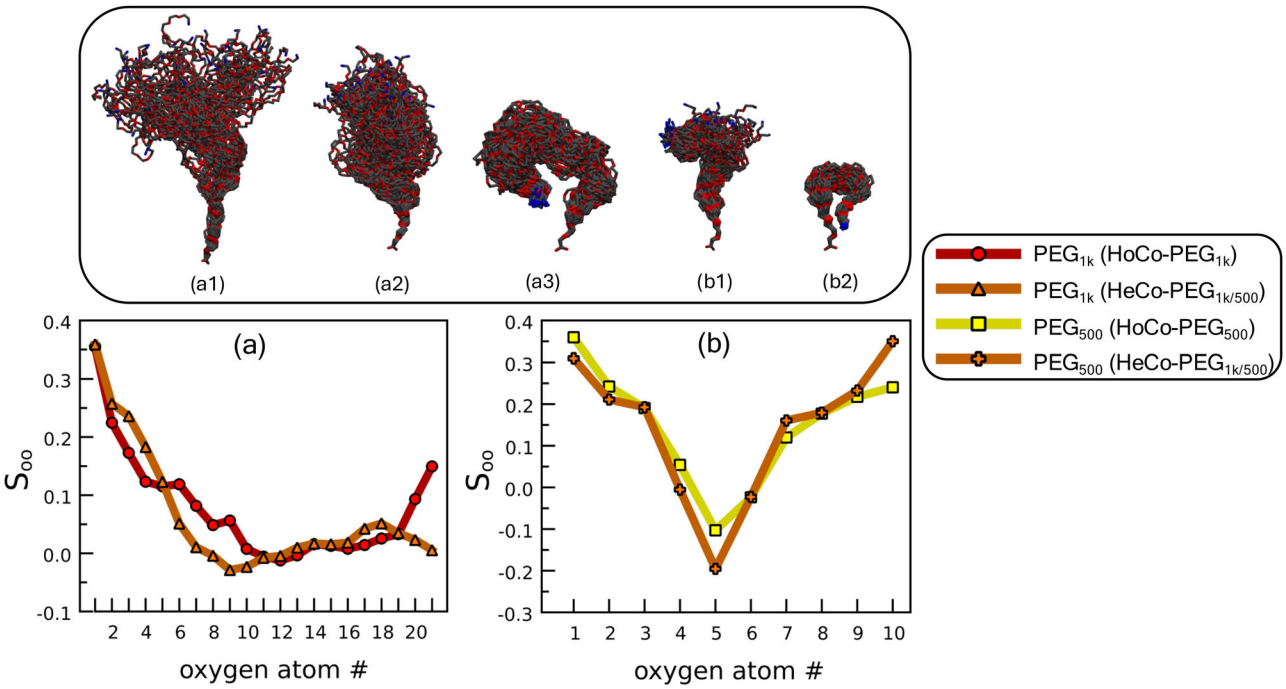

Fig. 8 | Order parameter and representative conformations of PEG chains across different coating morphologies. Order parameter for **a** PEG_{1k}-NH_3^+ chains in HoCo-PEG_{1k} and HeCo-$PEG_{1k/500}$ coating morphologies, **b** PEG_{500}-NH_3^+ chains in HoCo-PEG_{500} and HeCo-$PEG_{1k/500}$ coating morphologies. On the top, the most representative polymer conformations are superimposed over the last 50 ns of MD simulation for (a1, a2, a3) PEG_{1k}-NH_3^+ chains and (b1, b2) PEG_{500}-NH_3^+ chains.

chains in the HoCo-PEG_{500} coating (Fig. 7), suggesting that some steric suppression by longer PEG_{1k}-NH_3^+ chains over the shorter PEG_{500}-NH_3^+ chains might be happening. On the other hand, we find no significant changes in the RoG of PEG_{1k}-NH_3^+ chains by changing from HeCo-$PEG_{1k/500}$ to HoCo-PEG_{1k}, suggesting that the presentation of PEG_{1k}-NH_3^+ chains towards the bulk-water phase behaves similarly in both cases, where most of these chains acquire a brush conformation.

Order parameter of PEG chains. An effective polymeric coating depends on the proper balance of several coating parameters, which in turn directly impacts the dynamics of polymer chains within the coating corona, a critical aspect for tailoring nanosystem's properties.

Order parameter assessment, routinely adopted in biophysical studies of biomolecular assemblies[79], has also proven useful in assessing how tunable parameters like chain length, chemical nature, and composition of polymer coatings impact the overall ordering and conformation of their components within the polymeric corona[80–82].

Thus, we quantify the order parameter to identify the ordering of PEG chains in the system models according to Eq. (6).

$$S_{OO} = 0.5\left\langle \left(3\cos^2\theta - 1\right)\right\rangle \quad (6)$$

where θ is the angle formed between the principal axis normal to each DBT Fe_3O_4 (001) NP facet and the vectors formed by pairs of subsequent oxygen atoms along the PEG chain, starting from the vector formed between the two closest oxygen atoms in the two nearest PEG monomer units at the NP surface up to the vector formed between the two oxygen atoms in the PEG monomer units farther away from the NP surface. Average S_{oo} values are taken over all coating ligands and over the 50 ns long production phase.

Figure 8 depicts the order parameter of PEG_{1k}-NH_3^+ chains composing the HoCo-PEG_{1k} and HeCo-$PEG_{1k/500}$ coatings (Fig. 8a), and the PEG_{500}-NH_3^+ chains constituting the HoCo-PEG_{500} and HeCo-$PEG_{1k/500}$ coatings (Fig. 8b). In Fig. 8a, we observe a clear pattern of chain ordering near to the NP surface, which rapidly transitions into a random ordering regime up to the mid-length of NH_3^+-PEG_{1k} chains, acquiring mostly extended conformations with their chain's distal part exposed in the bulk-water phase (Fig. 8a1), enclosed within the outer region of the PEG corona (Fig. 8a2), or retained within the inner region of the PEG corona driven by H-bonds interaction between the terminal amine group and the available oxygen atoms on the NP surface (Fig. 8a3). From the tenth PEG monomeric unit on, PEG_{1k}–NH_3^+ chains behave quite similarly whatever homogeneous, or heterogeneous coating morphologies are adopted. However, a substantial difference can be spotted at the distal monomeric units of PEG_{1k}-NH_3^+ chains – the heterogeneous coating favors a more random orientation of the distal portion of PEG_{1k}-NH_3^+ chains while the homogeneous coating induces an enhanced chain ordering effect instead. This observation can be attributed to a less dense and crowded outer region within the heterogeneous PEG corona yielding an enhanced influx of water molecules at this region compared to the homogeneous coating, and therefore, higher molecular mobility of the distal PEG monomers in the PEG_{1k}-NH_3^+ chains.

Figure 8b reveals a quasi-symmetric order parameter observed around the fifth monomeric unit of PEG_{500}-NH_3^+ chains in both HoCo-PEG_{500} and HeCo-$PEG_{1k/500}$ coatings. We see a high ordering pattern of PEG_{500}-NH_3^+ chains near to the NP surface, which decreases rapidly to a random regime up to the mid-length of these chains, similarly to what we observe in the PEG_{1k}-NH_3^+ case (Fig. 8a). However, from the fifth monomeric unit on, we see an increasing ordering again regardless of whether a homogeneous or heterogeneous coating morphology is adopted, differing from what we observe in the PEG_{1k}-NH_3^+ chains.

Further analysis reveals that PEG_{500}-NH_3^+ chains not only can adopt extended conformations (Fig. 8b1) but also exhibit a considerable occurrence of mushroom conformations (Fig. 8b2) throughout the MD simulation trajectory. This mushroom conformation occurs to a higher extent compared to the extended ones in the case of PEG_{500}-NH_3^+ chains and is even more pronounced in the heterogeneous coating, where most of the positively charged PEG_X-NH_3^+ terminal groups are completely enclosed within the PEG corona either interacting with the oxygen atoms in the PEG monomer units or with the oxygen atoms exposed on the NP surface.

Lastly, RMSD analysis (Supplementary Note 3 and Supplementary Fig. 1) corroborates the observations above regarding the higher mobility of PEG_{1k}-NH_3^+ chains compared to PEG_{500}-NH_3^+ chains. Interestingly, we can also observe that the type of coating has a direct effect on the mobility of

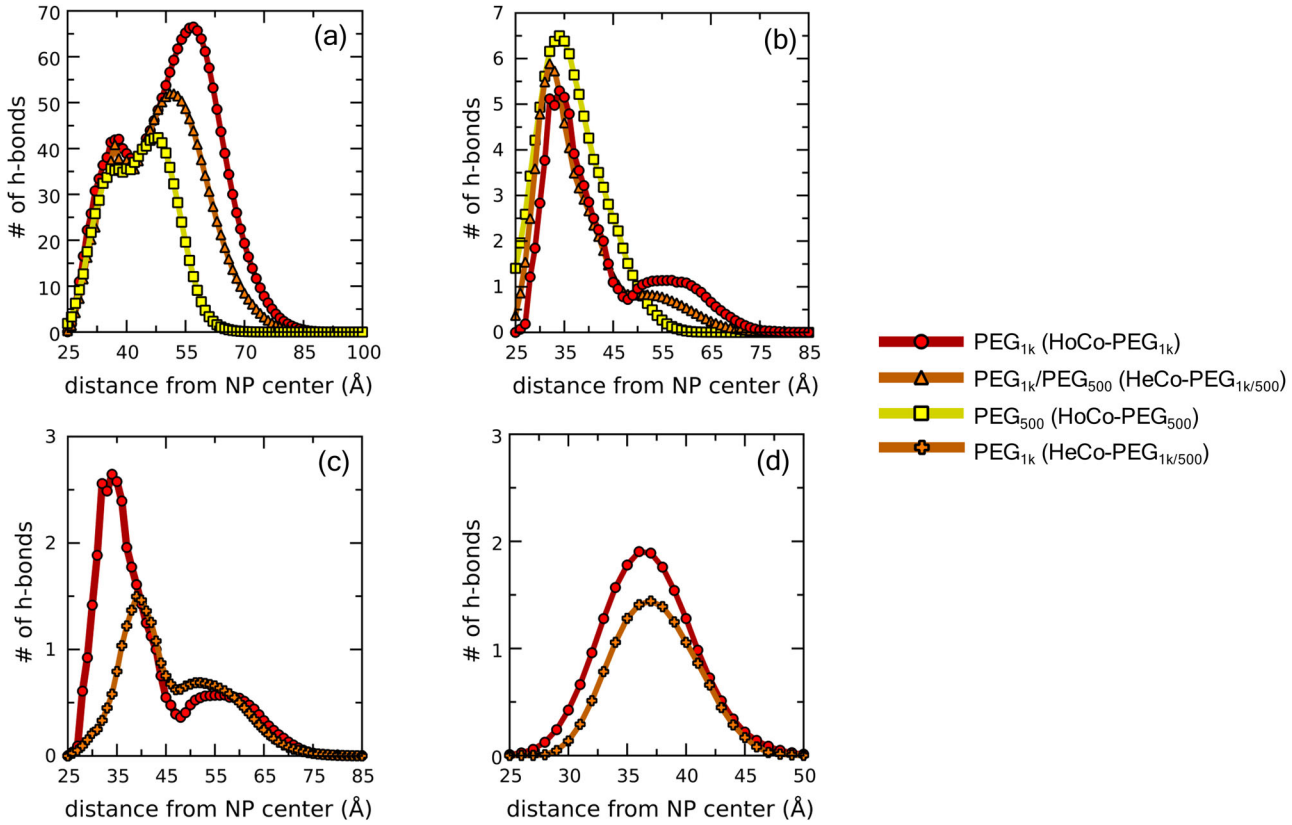

Fig. 9 | Polymer corona H-bonding across different PEG coating morphologies. Number of H-bond formations between **a** PEG_X-NH_3^+ chains and water molecules, **b** PEG_X-NH_3^+ terminal groups and PEG units of PEG_X-NH_3^+ chains, **c** PEG_{1k}-NH_3^+ terminal groups and PEG units of PEG_X-NH_3^+ chains, and **d** PEG_{1k}-NH_3^+ terminal groups and NP. For the sake of comparison between HoCo-PEG_{1k} and HeCo-$PEG_{1k/500}$ coatings in panels **c** and **d**, the number of H-bonds is normalized by the total number of coating chains based on their type and content.

these polymer chains throughout the simulations. In the HeCo-$PEG_{1k/500}$ coating, PEG_{1k}-NH_3^+ chains show greater mobility (higher RMSD values), while PEG_{500}-NH_3^+ chains become less mobile (lower RMSD values) compared to their counterparts in homogeneous coatings.

Polymer Corona H-Bonding analysis. A fundamental, and still open question revolves around the factors determining the ability of the polymeric coating layer surrounding NPs in controlling/suppressing the protein corona formation. An experimental assumption explaining the effectiveness of PEG coating layers in preventing the adsorption of proteins relies on the ability of these hydrophilic chains in binding a large amount of water molecules, through h-bonds, to their many available ether groups. PEG hence creates a highly viscous layer made of coordinated water molecules that shield the coated NP surface from further protein adsorption[83–88]. Thus, the verification and understanding, at molecular level, of the mechanism behind the formation of this experimentally hypothesized layer within the polymeric corona is of utmost relevance.

Therefore, we investigate the H-bonding among the nanosystem's components and surroundings across the three different coating compositions. Figure 9 shows the average number of H-bond formation occurring between the nanosystem's components and water molecules, and among the nanosystem's components, as a function of radial distance from the NP geometric center towards the bulk-water phase. The cumulative number of H-bonds in the radial profiles is then normalized by the simulation length to more accurately reflect the frequency of H-bonds occurring around the NP over time. We counted as an H-bond formation when both of these criteria are satisfied: I) the distance between H-bond donor and the H-acceptor is less than 3.0 Å; II) the supplementary angle to the one formed between the H-donor and H-acceptor heavy atoms, having the hydrogen atom as the vertex, is less than 20°.

For the sake of discussion, we split the polymeric coating corona in two main regions: the "inner region" of the PEG corona beginning at the shortest distance from the NP geometric center to its surface (25 Å) up to 45 Å from the NP center and an "outer region" of the PEG corona starting at 45 Å up to the bulk-water phase (at about 90 Å from the NP surface).

In Fig. 9a, we find that the tight polymeric packing within ~2 Å from the NP surface yields a reduced number of H-bonds formations between PEG_X-NH_3^+ chains and water molecules, regardless of the chain length or coating morphology employed. Then, we observe a rapid increase in the number of H-bonds within the inner PEG corona region (at about 10 Å from the NP surface), where no significant differences are observed among the different coatings. Moreover, as we move towards the outer PEG corona region, we identify that the higher the PEG_{1k}-NH_3^+ chain content, the greater the occurrence of H-bonds between the coating ligands and water molecules - in both HoCo-PEG_{1k} and HeCo-$PEG_{1k/500}$ morphologies, these H-bond formations extend beyond 50 Å farther from the NP surface. Interestingly, we observe that water molecules can form H-bonds with PEG chains across the whole coating layer, creating multiple layers of coordinated water molecules within the polymeric coating. For additional details on H-bond formation without anchoring group restraints, refer to Supplementary Note 4 and Supplementary Fig. 2.

Figure 9b presents the H-bond formation within the PEG corona between the chain's terminal group and the monomeric PEG units, for the three different coating morphologies. We observe that the maxima peaks of H-bonds occur within the inner polymeric corona region for all three cases. Among these, we observe that the HeCo-$PEG_{1k/500}$ morphology exhibits a slightly more internalized peak compared to the HoCo-PEG_{500} and HoCo-

PEG_{1k} morphologies. As we move from inner to the outer PEG corona region, there is a substantial decrease in the formation of H-bond up to 25 Å from the NP surface - beyond this point, the formation of H-bonds is practically extinguished in the HoCo-PEG_{500} case, whereas both the HeCo-$PEG_{1k/500}$ and HoCo-PEG_{1k} coatings still exhibit a considerable number of H-bonds extending up to 50 Å from the NP surface, with the latter morphology showing a more pronounced effect among all.

Figure 9c reveals that the HeCo-$PEG_{1k/500}$ coating yields a reduction of H-bonds between PEG_{1k}-NH_3^+ terminal groups and PEG monomers within the inner region of the PEG corona, while the HoCo-PEG_{1k} coating appears to enhance these interactions. A similar trend is found in Fig. 9d, where the HeCo-$PEG_{1k/500}$ coating shows a reduction in the overall number of H-bond formed between the positively charged PEG_{1k}-NH_3^+ terminal groups and the Fe_3O_4 NP core. The mechanism behind this is likely due to the steric effects of the longer PEG_{1k}-NH_3^+ chains over the shorter ones in the HeCo-$PEG_{1k/500}$ coating, increasing the packing/density of the latter near the NP surface and subsequently hampering the access of PEG_{1k}-NH_3^+ terminal groups in that region.

Despite the coating morphology adopted, the formation of H-bonds between PEG_X-NH_3^+ chains and water molecules are the most abundant. The higher the content of PEG_{1k}-NH_3^+ chains in the polymeric coating, the higher the H-bonds occurrence between the nanosystem's coating ligands and solvent molecules. Interestingly, our analysis also unveils the H-bonding formation among the nanosystem's components. This is mainly driven by intermolecular H-bonds between positively charged PEG_X-NH_3^+ terminal groups and either oxygen atoms of polymeric units of PEG or available oxygen atoms on the NP surface, in that order of relevance in contributing to the H-bonding formation within the PEG corona.

Discussion

In this work, we have presented a computational protocol for accurate and robust modeling of realistically-size Fe_3O_4 nanocube-shaped cores for designing of more complex experimentally relevant Fe_3O_4-based nanosystems.

Through our study, we have demonstrated the effectiveness of employing rescaled CLAY-based partial atomic charges and the mCLAY FF for Fe_3O_4 atoms, thereby expanding its applicability to the biomolecular CHARMM FF. This FF combination has shown satisfactory transferability across different dimensionalities of Fe_3O_4 materials, even at length scales beyond the reach of full quantum mechanics characterization, and their interactions with organic molecules of common chemical composition (H, C, O, and N atoms).

Furthermore, to highlight the practical implications of our work, we have built and simulated polymer coated Fe_3O_4-based nanosystems with different coating morphologies having the designed realistic-size 5 nm Fe_3O_4 NP as inorganic core. This case study allowed us to thoroughly investigate the interplay between polymer length and coating composition on key nanosystem properties, including polymeric coating thickness, polymer chain's order parameter, and H-bonding within the PEG corona.

Our findings have unveiled interesting trends: transitioning from HoCo-PEG_{500} to HeCo-$PEG_{1k/500}$ coatings leads to significant increase in coating thickness, while minimal impact on this parameter is found when changing from HeCo-$PEG_{1k/500}$ to HoCo-PEG_{1k} coating. Additionally, we observed distinct conformational preferences, with PEG_{500} chains favoring a mushroom-like shape and enhanced ordering, with most PEG_{500}-NH_3^+ terminal groups remaining internalized within the polymeric corona layer driven by an elevate number of H-bonds regardless of coating morphology. Rather, longer PEG_{1k} chains favor an extended conformation increasing randomness and disordering at the chain's distal portions towards the bulk-water accompanied by substantial decrease in H-bonds within the inner region of the polymer corona.

Interestingly, HeCo-$PEG_{1k/500}$ coating enhances even further disordering/mobility and loss of H-bonds of PEG_{1k} chains within the inner region of the polymer corona compared to the HoCo-PEG_{1k} coating. On the other hand, the HeCo-$PEG_{1k/500}$ coating enhances distal ordering and decreases mobility of PEG_{500} chains compared to the HoCo-PEG_{500} coating. These findings suggest the existence of a complex correlation between polymer length and coating morphology, highlighting the importance of the assessment of these parameters in polymer-coated nanosystem's designing.

In conclusion, this study provides a practical computational protocol and the necessary set of validated FF parameters for designing zero-dimensional cubic-shaped Fe_3O_4 structures interfacing biomolecular assemblies of common organic composition, backed by a systematic accuracy assessment via multi-level computational techniques. We envision that this work will serve as the basis for classical modeling of realistic-size Fe_3O_4-based nanosystems, paving the way for more efficient design of next-generation nanomaterials for nanomedical applications.

Methods

Density Functional Theory (DFT) calculations

Hybrid density functional theory calculations (HSE06)[89] were carried out using the CRYSTAL17 package[90]. For the validation against experimental data of the standard hybrid functional HSE06 as a robust theoretical approach to describe structural, electronic, and magnetic properties of magnetite system, please refer to ref. 91, where some of us also analyzed the effect of reducing the fraction of the exact exchange, in comparison with B3LYP and PBE + U calculations with different U values. The Kohn−Sham orbitals are expanded in Gaussian-type orbitals: the all-electron basis sets are H|511G(p1), C|6311G(d11), O|8411G(d1) (for magnetite oxygen atoms), O|8411G(d11) (for adsorbed molecules oxygen atoms), and Fe|86411G(d41). The convergence criteria of 10^{-6} Hartree and 4.5×10^{-4} Hartree/Bohr for total energy and forces, respectively, were used during self-consistent field calculations and geometry optimization, according to the scheme previously used for Fe_3O_4[37,50,91] For the 2D slab calculations, the irreducible Brillouin zone was sampled with a $3 \times 3 \times 1$ k-points grid generated with the Monkhorst-Pack scheme[92].

Density Functional Tight-Binding (DFTB) calculations

SCC-DFTB (short for Self-Consistent redistribution of Charges Density Functional Tight-Binding) calculations were carried out using the DFTB+ software[93]. SCC-DFTB is an approximate method that turns DFT into a tight-binding scheme and is derived from the second-order expansion of the Kohn-Sham DFT total energy with respect to the electron density fluctuations. The SCC-DFTB total energy can be written as in Eq. (7):

$$E_{tot} = \sum_{i}^{occ} \varepsilon_i + 1/2 \sum_{\alpha,\beta}^{N} \gamma_{\alpha,\beta} \Delta q_\alpha \Delta q_\beta + E_{rep} \quad (7)$$

where the first term is the sum of the one-electron energies ε_i coming from the diagonalization of the corresponding Kohn-Sham Hamiltonian matrix (where all three-center integrals are neglected), Δq_α and Δq_β are the induced charges on the atoms α and β, respectively, and $\gamma_{\alpha,\beta}$ is a Coulombic-like interaction potential. E_{rep} is a short-range pairwise repulsive potential. Neglecting three-center contributions from the Kohn-Sham Hamiltonian enables the use of integral tables, usually referred to as parameters. More details about the SCC-DFTB method can be found elsewhere[94,95]. DFTB will be used as shorthand for SCC-DFTB. For the Fe-Fe, Fe-H and Fe-C interactions, we used the "trans3d-0-1" set of parameters[96]. For the O-O, H-O, H-H, O-C, H-C and C-C interactions we used the "mio-1-1" set of parameters[97]. For the Fe-O interactions, we used the Slater-Koster files fitted by some of us previously[51], which can well reproduce the results for magnetite bulk and surfaces from HSE06 and PBE + U calculations. This refitting procedure of the Fe-O repulsive interactions in the "trans3d-0-1" parameter set, performed using DFT calculations with the PBE functional[51], enhanced the accuracy of the DFTB + U method in describing the lattice parameters, charge distribution, and electronic properties (including charge disproportion of Fe ions) for bulk Fe_3O_4 and its (001) surface[51]. The refitted DFTB parameter set was then also validated for their accuracy in describing adsorption energies, structural properties, and hydrogen-bond networks at

the Fe_3O_4 (001)/water interface, with DFTB + U results aligning closely with DFT/HSE06 predictions and experimental data[36]. Furthermore, these parameters yielded fair accuracy in predicting the structural, electronic, and magnetic properties of realistic-sized Fe_3O_4 nanoparticles, with results consistent with hybrid DFT/HSE06 calculations and experimental EXAFS spectra[37]. To further validate the "trans3d-0-1" and "mio-1-1" DFTB parameter sets in predicting structural and energetic properties at the Fe_3O_4/organic interface, a set of optimization calculations at low coverage regime of acetic acid (one dissociated or undissociated molecule per cell) on the DBT Fe_3O_4 (001) surface were conducted at the DFT/HSE06 and DFTB levels of theory. The resulting interatomic distances and adsorption energy values showed close agreement between DFT/HSE06 and DFTB methods, as reported in Supplementary Note 2 and Supplementary Table 6. To properly deal with the strong correlation effects among iron 3d electrons[98], DFTB + U with an effective U-J value of 3.5 eV was adopted according to our previous work on magnetite[35–37,45,50,51,91]. The convergence criterion of 10^{-4} a.u. for forces and the convergence threshold on the SCC procedure of 10^{-5} a.u. were used during geometry optimization together with conjugate gradient optimization algorithm. For the DFTB + U MD (DFTB MD) simulations, the Velocity Verlet driver was set with a timestep of 0.5 fs. The trajectories were obtained from 50 ps NVT runs at 300 K, using an Andersen thermostat. The convergence threshold on the SCC procedure of 5×10^{-3} a.u. was used during the MD production.

Classical Molecular Dynamics (MD) calculations

The bonded and non-bonded interactions were treated using the CHARMM potential energy functions implemented in the LAMMPS code (version 21 Nov 2023)[99,100], which can be written asin Eq. (8):

$$\begin{aligned} E_{total} &= E_{nonbond} + E_{bonded} \\ E_{nonbond} &= \sum_{nonbond} \left(4\epsilon_{ij} \left[\left(\frac{\sigma_{ij}}{r_{ij}}\right)^{12} - \left(\frac{\sigma_{ij}}{r_{ij}}\right)^{6} \right] + \frac{q_i q_j}{\epsilon r_{ij}} \right) \\ E_{bonded} &= \sum_{bonds} K_b \left(b - b_0\right)^2 + \sum_{angles} K_\theta \left(\theta - \theta_0\right)^2 + K_{ub} \left(r - r_{ub}\right)^2 \\ &\quad + \sum_{dihedral} K_\chi \left(1 + \cos\left(n\chi - \delta\right)\right) + \sum_{improper} K_{imp} \left(\varphi - \varphi_0\right)^2 \end{aligned} \tag{8}$$

in which arithmetic mixing rules were utilized to obtain the cross-term parameters for Lennard-Jones (12-6) interactions between unlike atoms as given in Eqs. (9) and (10)

$$\epsilon_{ij} = \left(\epsilon_i \epsilon_j\right)^{\frac{1}{2}} \tag{9}$$

$$\sigma_{ij} = \frac{1}{2}\left(\sigma_i + \sigma_j\right) \tag{10}$$

The long-range solver Particle-Particle Particle-Mesh (P3M)[101] handled the electrostatic interactions with a real-space cut-off of 12 Å smoothly switching forces to zero beyond 10 Å with a threshold of 10^{-5} for the error tolerance in forces. For 2D periodic MD simulations, we utilized the modified P3M solver using the slab correction implementation proposed by Yeh and Berkowitz[102] dumping out any spurious inter-slab interactions. The LJ (12-6) interactions were truncated with a 12 Å cut-off distance in the real space with forces smoothly switching to zero beyond 10 Å. Details on the CHARMM functional forms for the force switching scheme can be found elsewhere[103]. In all MD simulations reported herein, a minimization phase was carried out to minimize the total potential energy in all systems, followed by an equilibration phase 50 ns long. The MD production phase explored 150 ns of the phase space in the NVT ensemble at 303.15 K held constant by the Nosé-Hoover thermostat with a damping coefficient at 1.0 ps^{-1}, and the final analysis results were calculated over the last 50 ns of production phase. The SHAKE algorithm[104] was applied to constrain the O—H bonds and the H—O—H bond angles of water molecules, while all other bonded interactions in the systems were treated dynamically according to their respective FF parameters. Newton's equations of motion were integrated in time using the Velocity-Verlet integrator with a timestep of 2.0 fs.

Data availability

The authors declare that the main data supporting the findings of this study are available within the article and its Supplementary Information file.

Received: 18 April 2024; Accepted: 27 November 2024;
Published online: 25 January 2025

References

1. Pankhurst, Q. A., Connolly, J., Jones, S. K. & Dobson, J. Applications of magnetic nanoparticles in biomedicine. *J. Phys. D. Appl Phys.* **36**, R167–R181 (2003).
2. Laurent, S. et al. Magnetic iron oxide nanoparticles: synthesis, stabilization, vectorization, physicochemical characterizations, and biological applications. *Chem. Rev.* **108**, 2064–2110 (2008).
3. Gupta, A. K. & Gupta, M. Synthesis and surface engineering of iron oxide nanoparticles for biomedical applications. *Biomaterials* **26**, 3995–4021 (2005).
4. Colombo, M. et al. Biological applications of magnetic nanoparticles. *Chem. Soc. Rev.* **41**, 4306–4334 (2012).
5. Wu, W., Jiang, C. Z. & Roy, V. A. L. Designed synthesis and surface engineering strategies of magnetic iron oxide nanoparticles for biomedical applications. *Nanoscale* **8**, 19421–19474 (2016).
6. Yan, X. et al. Multifunctional biohybrid magnetite microrobots for imaging-guided therapy. *Sci. Robot.* **2**, eaaq1155 (2017).
7. Chow, E. K. H. & Ho, D. Cancer nanomedicine: From drug delivery to imaging. *Sci. Transl. Med.* **5**, 216rv4 (2013).
8. Park, J. et al. Ultra-large-scale syntheses of monodisperse nanocrystals. *Nat. Mater.* **3**, 891–895 (2004).
9. Kovalenko, M. V. et al. Fatty acid salts as stabilizers in size- and shape-controlled nanocrystal synthesis: the case of inverse spinel iron oxide. *J. Am. Chem. Soc.* **129**, 6352–6353 (2007).
10. Zhao, L. et al. Morphology-Controlled Synthesis of Magnetites with Nanoporous Structures and Excellent Magnetic Properties. *Chem. Mater.* **20**, 198–204 (2008).
11. Kim, D. et al. Synthesis of uniform ferrimagnetic magnetite nanocubes. *J. Am. Chem. Soc.* **131**, 454–455 (2009).
12. Li, X. et al. Rhombic dodecahedral Fe_3O_4: ionic liquid-modulated and microwave-assisted synthesis and their magnetic properties. *CrystEngComm* **13**, 6017 (2011).
13. Zhao, L. & Duan, L. Uniform Fe_3O_4 Octahedra with Tunable Edge Length – Synthesis by a Facile Polyol Route and Magnetic Properties. *Eur. J. Inorg. Chem.* **2010**, 5635–5639 (2010).
14. Santos-Carballal, D., Roldan, A., Grau-Crespo, R. & Leeuw, N. Hde A DFT study of the structures, stabilities and redox behaviour of the major surfaces of magnetite Fe_3O_4. *Phys. Chem. Chem. Phys.* **16**, 21082–21097 (2014).
15. Creutzburg, M. et al. Adsorption of oleic acid on magnetite facets. *Commun. Chem.* **5**, 1–9 (2022).
16. Sun, J. et al. Synthesis and characterization of biocompatible Fe_3O_4 nanoparticles. *J. Biomed. Mater. Res. A* **80**, 333–341 (2007).
17. Hou, Z., Liu, Y., Xu, J. & Zhu, J. Surface engineering of magnetic iron oxide nanoparticles by polymer grafting: synthesis progress and biomedical applications. *Nanoscale* **12**, 14957–14975 (2020).
18. Karaagac, O. & Köçkar, H. Improvement of the saturation magnetization of PEG coated superparamagnetic iron oxide nanoparticles. *J. Magn. Magn. Mater.* **551**, 169140 (2022).
19. Anbarasu, M., Anandan, M., Chinnasamy, E., Gopinath, V. & Balamurugan, K. Synthesis and characterization of polyethylene glycol (PEG) coated Fe_3O_4 nanoparticles by chemical co-precipitation method for biomedical applications. *Spectrochim. Acta A Mol. Biomol. Spectrosc.* **135**, 536–539 (2015).

20. Antarnusa, G. & Suharyadi, E. A synthesis of polyethylene glycol (PEG)-coated magnetite Fe_3O_4 nanoparticles and their characteristics for enhancement of biosensor. *Mater. Res. Express* **7**, 56103 (2020).
21. Peréz, D. LI et al. Synthesis of superparamagnetic iron oxide nanoparticles coated with polyethylene glycol as potential drug carriers for cancer treatment. *J. Nanopart. Res.* **26**, 2 (2024).
22. Radoń, A. et al. Influence of the modifiers in polyol method on magnetically induced hyperthermia and biocompatibility of ultrafine magnetite nanoparticles. *Sci. Rep.* **13**, 7860 (2023).
23. Patel, N. N., Mulla, N. R., Khot, V. M. & Patil, R. S. Anticancer activity of surface functionalized magnetite (Fe_3O_4) nanoparticles of polymer coating. *Emergent Mater*. https://doi.org/10.1007/s42247-023-00611-y (2023).
24. Barrera, C., Herrera, A., Zayas, Y. & Rinaldi, C. Surface modification of magnetite nanoparticles for biomedical applications. *J. Magn. Magn. Mater.* **321**, 1397–1399 (2009).
25. Thonglor, P. & Albutt, D. Polyethylene Glycol (PEG) Coated Magnetite Nanoparticles Prepared by Sol-Gel Method for Biotechnology Applications. *MSF* **1100**, 65–73 (2023).
26. Nguyen, D. T. & Kim, K.-S. Functionalization of magnetic nanoparticles for biomedical applications. *Korean J. Chem. Eng.* **31**, 1289–1305 (2014).
27. D'souza, A. A. & Shegokar, R. Polyethylene glycol (PEG): a versatile polymer for pharmaceutical applications. *Expert Opin. Drug Deliv.* **13**, 1257–1275 (2016).
28. Zhang, X., Wang, H., Ma, Z. & Wu, B. Effects of pharmaceutical PEGylation on drug metabolism and its clinical concerns. *Expert Opin. Drug Metab. Toxicol.* **10**, 1691–1702 (2014).
29. Boyer, C., Whittaker, M. R., Bulmus, V., Liu, J. & Davis, T. P. The design and utility of polymer-stabilized iron-oxide nanoparticles for nanomedicine applications. *NPG Asia Mater.* **2**, 23–30 (2010).
30. Rowan, A. D., Patterson, C. H. & Gasparov, L. V. Hybrid density functional theory applied to magnetite: Crystal structure, charge order, and phonons. *Phys. Rev. B* **79**, 205103 (2009).
31. Noh, J., Osman, O. I., Aziz, S. G., Winget, P. & Brédas, J.-L. A density functional theory investigation of the electronic structure and spin moments of magnetite. *Sci. Technol. Adv. Mater.* **15**, 44202 (2014).
32. Righi, G., Fabris, S. & Piccinin, S. Oxygen Evolution Reaction on the Fe_3O_4 (001) Surface: Theoretical Insights into the Role of Terminal and Bridging Oxygen Atoms. *J. Phys. Chem. C.* **125**, 18752–18761 (2021).
33. Meier, M. et al. Water agglomerates on Fe_3O_4(001). *Proc. Natl Acad. Sci. USA* **115**, E5642–E5650 (2018).
34. Bourgund, A. et al. Influence of local defects on the dynamics of O–H bond breaking and formation on a magnetite surface. *J. Phys. Chem. C.* **123**, 19742–19747 (2019).
35. Liu, H., Siani, P., Bianchetti, E., Zhao, J. & Di Valentin, C. Multiscale simulations of the hydration shells surrounding spherical Fe_3O_4 nanoparticles and effect on magnetic properties. *Nanoscale* **13**, 9293–9302 (2021).
36. Liu, H., Bianchetti, E., Siani, P. & Di Valentin, C. Insight into the interface between Fe_3O_4 (001) surface and water overlayers through multiscale molecular dynamics simulations. *J. Chem. Phys.* **152**, 124711 (2020).
37. Liu, H. & Di Valentin, C. Shaping Magnetite Nanoparticles from First Principles. *Phys. Rev. Lett.* **123**, 186101 (2019).
38. Gürsoy, E., Vonbun-Feldbauer, G. B. & Mei, R. H. Oxidation-State Dynamics and Emerging Patterns in Magnetite. *J. Phys. Chem. Lett.* **14**, 6800–6807 (2023).
39. Konuk, M., Sellschopp, K., Vonbun-Feldbauer, G. B. & Mei, R. H. Modeling charge redistribution at magnetite interfaces in empirical force fields. *J. Phys. Chem. C.* **125**, 4794–4805 (2021).
40. Grasso, G. et al. Cell Penetrating Peptide Adsorption on Magnetite and Silica Surfaces: A Computational Investigation. *J. Phys. Chem. B* **119**, 8239–8246 (2015).
41. Qiang, L. et al. Molecular dynamics simulations of the interaction between Fe_3O_4 and biocompatible polymer. *Colloids Surf. A: Physicochemical Eng. Asp.* **456**, 62–66 (2014).
42. Qiang, L. et al. Atomic-scale interactions of the interface between chitosan and Fe_3O_4. *Colloids Surf. A* **419**, 125–132 (2013).
43. Gonçalves, T. A. R., Silva, L. A., Pereira, A. M., Peres, A. E. C. & Correia, J. C. G. Advancing iron ore slimes magnetic separation with functionalized Nanoparticles: Molecular insights from free energy simulations. *Appl. Surf. Sci.* **642**, 158498 (2024).
44. Kundu, T. K., Rao, K. H. & Parker, S. C. Atomistic simulation studies of magnetite surface structures and adsorption behavior in the presence of molecular and dissociated water and formic acid. *J. Colloid Interface Sci.* **295**, 364–373 (2006).
45. Siani, P., Bianchetti, E., Liu, H. & Di Valentin, C. Parametrization of the Fe-Owater cross-interaction for a more accurate Fe_3O_4/water interface model and its application to a spherical Fe_3O_4 nanoparticle of realistic size. *J. Chem. Phys.* **154**, 34702 (2021).
46. Mahmood, A. U., Rizvi, M. H., Tracy, J. B. & Yingling, Y. G. Solvent Effects in Ligand Stripping Behavior of Colloidal Nanoparticles. *ACS Nano* **17**, 13319–13332 (2023).
47. Kerisit, S. Water structure at hematite–water interfaces. *Geochim. Cosmochim. Acta* **75**, 2043–2061 (2011).
48. Cygan, R. T., Liang, J.-J. & Kalinichev, A. G. Molecular models of hydroxide, oxyhydroxide, and clay phases and the development of a general force field. *J. Phys. Chem. B* **108**, 1255–1266 (2004).
49. Pentcheva, R. et al. Jahn-Teller stabilization of a 'polar' metal oxide surface: Fe_3O_4(001). *Phys. Rev. Lett.* **94**, 126101 (2005).
50. Liu, H. & Di Valentin, C. Bulk-terminated or reconstructed Fe_3O_4(001) surface: water makes a difference. *Nanoscale* **10**, 11021–11027 (2018).
51. Liu, H., Seifert, G. & Di Valentin, C. An efficient way to model complex magnetite: Assessment of SCC-DFTB against DFT. *J. Chem. Phys.* **150**, 94703 (2019).
52. Bianchetti, E., Perilli, D. & Di Valentin, C. Improving the Oxygen Evolution Reaction on Fe_3O_4(001) with Single-Atom Catalysts. *ACS Catal.* **13**, 4811–4823 (2023).
53. Jewett, A. I. et al. Moltemplate: A Tool for Coarse-Grained Modeling of Complex Biological Matter and Soft Condensed Matter Physics. *J. Mol. Biol.* **433**, 166841 (2021).
54. Amstad, E., Gillich, T., Bilecka, I., Textor, M. & Reimhult, E. Ultrastable iron oxide nanoparticle colloidal suspensions using dispersants with catechol-derived anchor groups. *Nano Lett.* **9**, 4042–4048 (2009).
55. Gutiérrez, I. S. et al. Parametrization of halogen bonds in the CHARMM general force field: Improved treatment of ligand-protein interactions. *Bioorg. Med Chem.* **24**, 4812–4825 (2016).
56. Vanommeslaeghe, K. et al. CHARMM general force field: A force field for drug-like molecules compatible with the CHARMM all-atom additive biological force fields. *J. Comput Chem.* **31**, 671–690 (2010).
57. Vanommeslaeghe, K. & MacKerell, A. D. Automation of the CHARMM General Force Field (CGenFF) I: bond perception and atom typing. *J. Chem. Inf. Model* **52**, 3144–3154 (2012).
58. Siani, P. & Di Valentin, C. Effect of dopamine-functionalization, charge and pH on protein corona formation around TiO_2 nanoparticles. *Nanoscale* **14**, 5121–5137 (2022).
59. Siani, P., Frigerio, G., Donadoni, E. & Di Valentin, C. Molecular dynamics simulations of cRGD-conjugated PEGylated TiO_2 nanoparticles for targeted photodynamic therapy. *J. Colloid Interface Sci.* **627**, 126–141 (2022).

60. MacKerell, A. D. et al. All-atom empirical potential for molecular modeling and dynamics studies of proteins. *J. Phys. Chem. B* **102**, 3586–3616 (1998).
61. Beglov, D. & Roux, B. Finite representation of an infinite bulk system: Solvent boundary potential for computer simulations. *J. Chem. Phys.* **100**, 9050–9063 (1994).
62. Noskov, S. Y. & Roux, B. Control of ion selectivity in LeuT: two Na^+ binding sites with two different mechanisms. *J. Mol. Biol.* **377**, 804–818 (2008).
63. Kim, S. et al. CHARMM-GUI ligand reader and modeler for CHARMM force field generation of small molecules. *J. Comput Chem.* **38**, 1879–1886 (2017).
64. Jo, S., Kim, T., Iyer, V. G. & Im, W. CHARMM-GUI: a web-based graphical user interface for CHARMM. *J. Comput Chem.* **29**, 1859–1865 (2008).
65. Motta, S., Siani, P., Levy, A. & Di Valentin, C. Exploring the drug loading mechanism of photoactive inorganic nanocarriers through molecular dynamics simulations. *Nanoscale* **13**, 13000–13013 (2021).
66. Motta, S. et al. Metadynamics simulations for the investigation of drug loading on functionalized inorganic nanoparticles. *Nanoscale* **15**, 7909–7919 (2023).
67. Gamba, O. et al. Adsorption of Formic Acid on the Fe_3O_4 (001) Surface. *J. Phys. Chem. C.* **119**, 20459–20465 (2015).
68. Arndt, B. et al. Carboxylic acid induced near-surface restructuring of a magnetite surface. *Commun. Chem.* **2**, 1–8 (2019).
69. Angelis, F. D., Fantacci, S. & Gebauer, R. Simulating dye-sensitized TiO_2 heterointerfaces in explicit solvent: Absorption spectra, energy levels, and dye desorption. *J. Phys. Chem. Lett.* **2**, 813–817 (2011).
70. Siani, P., Motta, S., Ferraro, L., Dohn, A. O. & Di Valentin, C. Dopamine-Decorated TiO_2 Nanoparticles in Water: A QM/MM vs an MM Description. *J. Chem. Theory Comput.* **16**, 6560–6574 (2020).
71. Zhang, X. et al. Conformation-Dependent Coordination of Carboxylic Acids with Fe_3O_4 Nanoparticles Studied by ATR-FTIR Spectral Deconvolution. *Langmuir* **35**, 5770–5778 (2019).
72. Miyazaki, T., Tange, T., Kawashita, M. & Jeyadevan, B. Structural control of magnetite nanoparticles for hyperthermia by modification with organic polymers: effect of molecular weight. *RSC Adv.* **10**, 26374–26380 (2020).
73. Wang, J. et al. Modulating the toxicity of engineered nanoparticles by controlling protein corona formation: Recent advances and future prospects. *Sci. Total Environ.* **914**, 169590 (2024).
74. Bashiri, G. et al. Nanoparticle protein corona: from structure and function to therapeutic targeting. *Lab Chip* **23**, 1432–1466 (2023).
75. Abstiens, K., Gregoritza, M. & Goepferich, A. M. Ligand Density and Linker Length are Critical Factors for Multivalent Nanoparticle-Receptor Interactions. *ACS Appl Mater. Interfaces* **11**, 1311–1320 (2019).
76. Krpetić, Z. et al. High-resolution sizing of monolayer-protected gold clusters by differential centrifugal sedimentation. *ACS Nano* **7**, 8881–8890 (2013).
77. Franco-Ulloa, S. et al. NanoModeler CG: A Tool for Modeling and Engineering Functional Nanoparticles at a Coarse-Grained Resolution. *J. Chem. Theory Comput.* **19**, 1582–1591 (2023).
78. Rubinstein, M. & Colby, R. H. *Polymer Physics*. (Oxford University PressOxford, 2003). https://doi.org/10.1093/oso/9780198520597.001.0001.
79. Douliez, J. P., Léonard, A. & Dufourc, E. J. Restatement of order parameters in biomembranes: calculation of C-C bond order parameters from C-D quadrupolar splittings. *Biophys. J.* **68**, 1727–1739 (1995).
80. Liu, A. Y., Emamy, H., Douglas, J. F. & Starr, F. W. Effects of chain length on the structure and dynamics of semidilute nanoparticle–polymer composites. *Macromolecules* **54**, 3041–3051 (2021).
81. Dahal, U. & Dormidontova, E. E. Chain conformation and hydration of polyethylene oxide grafted to gold nanoparticles: curvature and chain length effect. *Macromolecules* **53**, 8160–8170 (2020).
82. Dahal, U., Wang, Z. & Dormidontova, E. E. Hydration of Spherical PEO-Grafted Gold Nanoparticles: Curvature and Grafting Density Effect. *Macromolecules* **51**, 5950–5961 (2018).
83. Ozer, I. & Chilkoti, A. Site-Specific and Stoichiometric Stealth Polymer Conjugates of Therapeutic Peptides and Proteins. *Bioconjug Chem.* **28**, 713–723 (2017).
84. Parrott, M. C. & DeSimone, J. M. Relieving PEGylation. *Nat. Chem.* **4**, 13 (2011).
85. García, K. P. et al. Zwitterionic-Coated "Stealth" Nanoparticles for Biomedical Applications: Recent Advances in Countering Biomolecular Corona Formation and Uptake by the Mononuclear Phagocyte System. *Small* **10**, 2516–2529 (2014).
86. Keefe, A. J. & Jiang, S. Poly(zwitterionic)protein conjugates offer increased stability without sacrificing binding affinity or bioactivity. *Nat. Chem.* **4**, 59 (2011).
87. Shafaei, N., Khorshidi, S. & Karkhaneh, A. The immune-stealth polymeric coating on drug delivery nanocarriers: In vitro engineering and in vivo fate. *J. Biomater. Appl.* **38**, 159–178 (2023).
88. Malachowski, T. & Hassel, A. Engineering nanoparticles to overcome immunological barriers for enhanced drug delivery. *Engineered Regen.* **1**, 35–50 (2020).
89. Krukau, A. V., Vydrov, O. A., Izmaylov, A. F. & Scuseria, G. E. Influence of the exchange screening parameter on the performance of screened hybrid functionals. *J. Chem. Phys.* **125**, 224106 (2006).
90. Dovesi, R. et al. Quantum-mechanical condensed matter simulations with CRYSTAL. *WIREs Comput. Mol. Sci.* e1360, https://doi.org/10.1002/wcms.1360 (2018).
91. Liu, H. & Di Valentin, C. Band Gap in Magnetite above Verwey Temperature Induced by Symmetry Breaking. *J. Phys. Chem. C. Nanomater Interfaces* **121**, 25736–25742 (2017).
92. Monkhorst, H. J. & Pack, J. D. Special points for Brillouin-zone integrations. *Phys. Rev. B* **13**, 5188–5192 (1976).
93. Aradi, B., Hourahine, B. & Frauenheim, T. DFTB+, a Sparse Matrix-Based Implementation of the DFTB Method. *J. Phys. Chem. A* **111**, 5678–5684 (2007).
94. Foulkes, W. M. C. & Haydock, R. Tight-binding models and density-functional theory. *Phys. Rev. B* **39**, 12520–12536 (1989).
95. Elstner, M. & Seifert, G. Density functional tight binding. *Philos. Trans. R. Soc. A Math. Phys. Eng. Sci.* **372**, 20120483 (2014).
96. Zheng, G. et al. Parameter calibration of transition-metal elements for the spin-polartaed self-consistent-charge density-functional tight-binding (DFTB) Method: Sc, Ti, Fe, Co, and Ni. *J. Chem. Theory Comput.* **3**, 1349–1367 (2007).
97. Elstner, M. et al. Self-consistent-charge density-functional tight-binding method for simulations of complex materials properties. *Phys. Rev. B* **58**, 7260–7268 (1998).
98. Hourahine, B. et al. Self-interaction and strong correlation in DFTB. *J. Phys. Chem. A* **111**, 5671–5677 (2007).
99. Plimpton, S. Fast Parallel Algorithms for Short-Range Molecular Dynamics. *J. Comput Phys.* **117**, 1–19 (1995).
100. Thompson, A. P. et al. LAMMPS - a flexible simulation tool for particle-based materials modeling at the atomic, meso, and continuum scales. *Comput Phys. Commun.* **271**, 108171 (2022).
101. Hockney, R. W. & Eastwood, J. W. *Computer Simulation Using Particles*. (CRC Press, 2021). https://doi.org/10.1201/9780367806934.
102. Yeh, I.-C. & Berkowitz, M. L. Ewald summation for systems with slab geometry. *J. Chem. Phys.* **111**, 3155 (1999).
103. Steinbach, P. J. & Brooks, B. R. New spherical-cutoff methods for long-range forces in macromolecular simulation. *J. Comput. Chem.* **15**, 667–683 (1994).

104. Ryckaert, J.-P., Ciccotti, G. & Berendsen, H. J. C. Numerical integration of the cartesian equations of motion of a system with constraints: molecular dynamics of n-alkanes. *J. Comput. Phys.* **23**, 327–341 (1977).

Acknowledgements

The authors are grateful to Prof. Francesca Re, Prof. Roberto Fiammengo, and Chiara Daldossi for fruitful discussion and to Lorenzo Ferraro for his technical support. The research leading to these results has received funding from the European Union - NextGenerationEU through the Italian Ministry of University and Research under PNRR - M4C2-I1.3 Project PE_00000019 “HEAL ITALIA” to Prof. Cristiana Di Valentin CUP H43C22000830006 of University of Milano Bicocca.

Author contributions

Paulo Siani: Methodology, Data curation, Validation, Formal analysis, Writing – original draft. Enrico Bianchetti: Data curation, Formal analysis. Cristiana Di Valentin: Conceptualization, Methodology, Funding acquisition, Resources, Supervision, Writing – review & editing. All authors reviewed and approved the manuscript.

Competing interests

The authors declare no competing interests.

Additional information

Supplementary information The online version contains supplementary material available at https://doi.org/10.1038/s41524-024-01476-3.

Correspondence and requests for materials should be addressed to Paulo Siani or Cristiana Di Valentin.